NAVAL POSTGRADUATE SCHOOL

MONTEREY, CALIFORNIA

THESIS

DETERMINATION OF DYNAMIC RESPONSE OF CERAMICS AND CERAMIC-METALS UNDER SHOCK COMPRESSION AND SPALL

by

Chin Wah John Tan

December 2010

Thesis Co-Advisors:	Young Kwon
	Jose O. Sinibaldi
Second Reader:	Robert S. Hixson

Approved for public release; distribution is unlimited

THIS PAGE INTENTIONALLY LEFT BLANK

1. AGENCY USE ONLY *(Leave blank)*	2. REPORT DATE December 2010	3. REPORT TYPE AND DATES COVERED Master's Thesis
4. TITLE AND SUBTITLE Determination of Dynamic Response of Ceramics and Ceramic-Metals Under Shock Compression and Spall		5. FUNDING NUMBERS
6. AUTHOR(S) Chin Wah John Tan		
7. PERFORMING ORGANIZATION NAME(S) AND ADDRESS(ES) Naval Postgraduate School Monterey, CA 93943-5000		8. PERFORMING ORGANIZATION REPORT NUMBER
9. SPONSORING /MONITORING AGENCY NAME(S) AND ADDRESS(ES) N/A		10. SPONSORING/MONITORING AGENCY REPORT NUMBER

11. SUPPLEMENTARY NOTES The views expressed in this thesis are those of the author and do not reflect the official policy or position of the Department of Defense or the U.S. Government. IRB Protocol number _____N/A_____.

12a. DISTRIBUTION / AVAILABILITY STATEMENT Approved for public release; distribution is unlimited	12b. DISTRIBUTION CODE

13. ABSTRACT (maximum 200 words)

A new composite armor concept that encompasses an extremely hard first layer to deform the projectile, an orthotropic second layer to slow down the shock wave propagation, a third porous layer to absorb the shock wave energy through PV-work, and a fourth layer to provide confinement for the porous medium has been conceived. Ceramic Corbit-98 and Ceramet Tungsten Carbide were selected as candidate materials for the first layer and these were the focus of this research. Dynamic loading responses of the material studied were determined through planar impact experiment conducted on a single stage light-gas gun at NPS Impact Physic Lab. Impact velocities ranged from 0.2 to 0.35 km/s. The impactor material for asymmetric experiments was z-cut single crystal sapphire. Diagnostic used included a VISAR system, to measure particle velocities, PZT pins to measure onset of impact, and contact pins to measure impactor velocities and tilt angles. Through this study, dynamic loading response of ceramic Corbit-98 and ceramet tungsten carbide were determined. The Hugoniot EOS for Corbit-98 ceramic and GC-915 tungsten carbide were measured to be $U_s = 0.959 * U_p + 10.57$ and $U_s = 10.2 * U_p + 5.42$, respectively. The Hugoniot Elastic Limit (HEL) of GC-915 was found to be 0.935 GPa and spall strength of approximately 2 GPa was also measured.

14. SUBJECT TERMS Ceramet, Ceramic, shock properties, Hugoniot equation of state, Hugoniot elastic limit, sound speed, single stage gas gun.			15. NUMBER OF PAGES 93
			16. PRICE CODE

17. SECURITY CLASSIFICATION OF REPORT Unclassified	18. SECURITY CLASSIFICATION OF THIS PAGE Unclassified	19. SECURITY CLASSIFICATION OF ABSTRACT Unclassified	20. LIMITATION OF ABSTRACT UU

THIS PAGE INTENTIONALLY LEFT BLANK

DETERMINATION OF DYNAMIC RESPONSE OF CERAMICS AND CERAMIC-METALS UNDER SHOCK COMPRESSION AND SPALL

Chin Wah John Tan
Military Expert 5, Singapore Army
B.S., University of Western Australia, 2004

Submitted in partial fulfillment of the
requirements for the degree of

**MASTER OF SCIENCE IN ENGINEERING SCIENCE
(MECHANICAL ENGINEERING)**

from the

**NAVAL POSTGRADUATE SCHOOL
December 2010**

Author: Chin Wah John Tan

Approved by: Young Kwon
                 Thesis Co-Advisor

                 Jose O. Sinibaldi
                 Thesis Co-Advisor

                 Prof. Robert S. Hixson
                 Second Reader

                 Knox T. Millsaps
                 Chairman, Department of Mechanical and Aerospace Engineering

THIS PAGE INTENTIONALLY LEFT BLANK

ABSTRACT

A new composite armor concept that encompasses an extremely hard first layer to deform the projectile, an orthotropic second layer to slow down the shock wave propagation, a third porous layer to absorb the shock wave energy through PV-work, and a fourth layer to provide confinement for the porous medium has been conceived. Ceramic Corbit-98 and Ceramet Tungsten Carbide were selected as candidate materials for the first layer and these were the focus of this research. Dynamic loading responses of the material studied were determined through planar impact experiment conducted on a single stage light-gas gun at NPS Impact Physic Lab. Impact velocities ranged from 0.2 to 0.35 km/s. The impactor material for asymmetric experiments was z-cut single crystal sapphire. Diagnostics used included a VISAR system, to measure particle velocities, PZT pins to measure onset of impact, and contact pins to measure impactor velocities and tilt angles. Through this study, dynamic loading response of ceramic Corbit-98 and ceramet tungsten carbide were determined. The Hugoniot EOS for Corbit-98 ceramic and GC-915 tungsten carbide were measured to be $U_s = 0.959 * U_p + 10.57$ and $U_s = 10.2 * U_p + 5.42$, respectively. The Hugoniot Elastic Limit (HEL) of GC-915 was found to be 0.935 GPa and spall strength of approximately 2 GPa was also measured.

THIS PAGE INTENTIONALLY LEFT BLANK

TABLE OF CONTENTS

LIST OF FIGURES

LIST OF TABLES

THIS PAGE INTENTIONALLY LEFT BLANK

LIST OF ACRONYMS AND ABBREVIATIONS

AL6061   Aluminum alloy 6061

EFP   Explosively formed projectiles

GPa   Gigapascals = 10^9 N/m^2

HEL   Hugoniot elastic limit

LANL   Los Alamos National Lab

NPS   Naval Postgraduate School

PDV   Photonic Doppler Velocimetry

PZT   piezoelectric

RHA   Rolled Homogeneous Armor

SNL   Sandia National Lab

VISAR   Velocity Interferometer System for Any Reflector

THIS PAGE INTENTIONALLY LEFT BLANK

ACKNOWLEDGMENTS

I would like to take this opportunity to thank my thesis advisor; Prof Jose O. Sinibaldi, Professor Robert S. Hixson and Professor Young Kwon for their patience, guidance and support given throughout the course of my study here at NPS. Without their help, I would not have been able to successfully complete the thesis in such a short span of time.

Next, I would also like to thank my colleague, LT Jonathan Garner for showing me the ropes and providing me with insights to the preparation of the experimental setups. I would also like to thank Leonel, Elliot and Laurel for all the help rendered during the preparation of all the experiments and the time spent in the lab would not have been as enjoyable if not for them. Of course, all wouldn't have been made possible without the help of the support staff George, at every crucial moment.

Finally, I must thank my wife, May, for her constant support and encouragement during the course of my tour in NPS.

THIS PAGE INTENTIONALLY LEFT BLANK

I.   INTRODUCTION

A.   BACKGROUND

This thesis is a continuation of previous Naval Postgraduate School (NPS) research performed by Denzel (2010) to investigate the shock properties of ceramic Corbit-98 (98% Alumina) and above that, a new investigation into Tungsten-Carbide in a Cobalt matrix (WC/Co) ceramet.

The main motivation of this research is based upon the concept of employing a layered structure (Ong, 2009) for personnel armor. This layered structure stops the projectile in a series of stages as shown graphically in Figure 1: first, a projectile encounters a high yield strength, high impedance material which causes considerable plastic deformation of the projectile, which serves twofold purposes: a) to transfer projectile kinetic energy into internal energy of the projectile during the plastic flow, and b) reduces the amplitude of the shock waves produced by increasing the cross-sectional area of the projectile; second, rapidly spreading the shock wave created by the projectile laterally with the use of special orthotropic composite material; third, converting the remnants of the kinetic energy from the impact into waste heat with the use of porous or phase changing materials; and fourth, a final stopping layer made of conventional armor materials such as Kevlar. The success of this multi-layered structure for personnel armor will allow potential space and weight savings due to the associated better specific (per unit mass) penetration resistance abilities. The focus of this thesis, is on the first layer (high strength and high impedance), which will be investigated in detail.
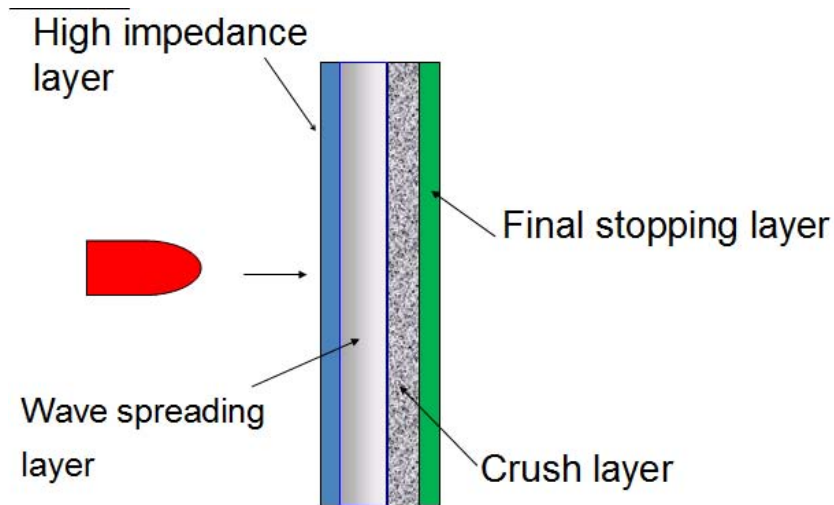
Figure 1.   Graphical illustration of new layered armor concept (From Ong, 2009)

To help disperse the momentum of the projectile, it needs to be plastically deformed causing the projectile kinetic energy to be converted into internal energy and waste heat. In order for that to happen, the armor must possess a much higher yield strength so thereby causing the projectile to yield before the armor. This yielding point is at the onset of plastic deformation, and is also known as Hugoniot Elastic Limit (HEL) in shock physics.

A high HEL is critical for any armor protection material to cause significant deformation to occur in the projectile. Therefore, the material of choice for the first layer would be a material of very high HEL. Due to the high HEL of Ceramic Corbit-98 (8.27 GPa), it was selected as the choice of material to be studied. Tungsten Carbide is a metal alloy with attractive compressive and tensile strength properties, making it ideally suited for use as a protective element to mitigate shock-induced effects and was therefore chosen as the second material to study for the purpose of this thesis.

The prime objective of this research is to experimentally determine the HEL WC/Co alloy to determine their suitability as the Momentum Dispersion layer.

B.   LITERATURE RESEARCH

1.   Ballistic Protection

At present, most of the research on armor is based on finding a single material that can resist penetration from projectiles. The most common choice of material used is Rolled Homogeneous Armor (RHA), which is a type of hardened steel alloy with a HEL of between 2 to 3 GPa. A major drawback of steel is its high density, which causes it to be an impractical candidate for body armor due to the weight. However with new research and development, the material candidates evolved to the use of technical ceramics (e.g., Aluminum Oxide, Boron Carbide, Aluminum Nitrate and others for their high strength property at relatively lightweight. The use of even more advance materials (e.g., Kevlar Fiber- Reinforced Polymers [KFRP]), Carbon Fiber Reinforced Polymers (CFRP), and Aramid or Polyethylene woven fabric composites has also become more common. Figure 2 shows a brief classification of these advanced composites.
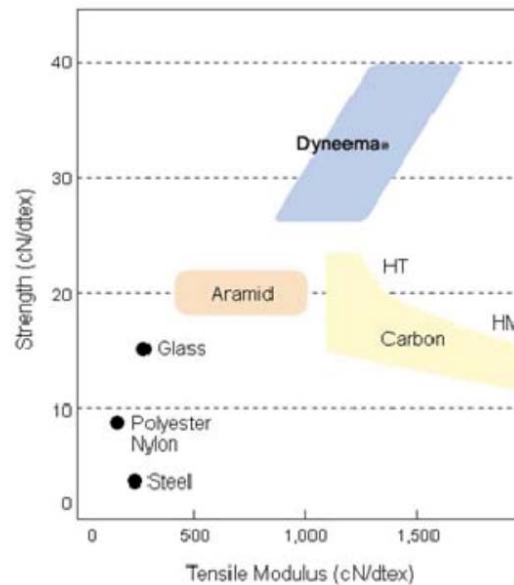
Figure 2.   Relative strength/tensile modulus of advanced fiber composites (From Ong, 2009)

Such evolution of protection technology has had varying success in the defeat of a certain class of projectiles and it became evident that such existing technologies may have reached a plateau in the development of body armor.

2. Impetus for Ongoing Research

With quickly evolving projectile threats and stagnating development of body armor, the need for new armor protection concepts to break through the current paradigm becomes clear. Much interest has been shown in the development of armor protection using layered armor as demonstrated by Robbins, Ding, and Gupta (2004). Gupta and Ding (2002) demonstrated the use of wave spreading material to dissipate the compressive forces of the incoming projectile within a microsecond timescale. Wilkins (1978) have also shown the effectiveness of ceramics in plastically deforming the projectile thus defeating it from the onset and preventing extensive damage to the lower layers of armor. Herrman (1969) has also demonstrated the effectiveness of porous materials in absorbing energy during shock compression. All the works mentioned above have shown promise when used in individual layers, but there is still a need to put these concepts together as a multi-layered armor system, with each layer playing a specific role in defeating projectile penetration.

Poh (2008) has shown the feasibility of composite layered armor construction consisting relatively dissimilar materials with each material aiding to resist penetration with specific properties. The first layer of the composite layered armor he modeled consist of a high strength layer to plastically defeat the projectile, and a wave spreading idealized material as a second layer to laterally dissipate the compressive shock waves and finally a porous layer to assist in absorbing the residual energy. Through numerical simulation using the Autodyn® hydrodynamic code, he was able to demonstrate the feasibility of a composite layered construction, in the sequence mentioned above, to resist the impact of a projectile, which performed better than an AISI 4340 armor grade high strength steel plate of equivalent thickness. Figure 3 shows results from his simulations where AISI 4340 steel armor is perforated as compared a composite armor with just minimal penetration.

4
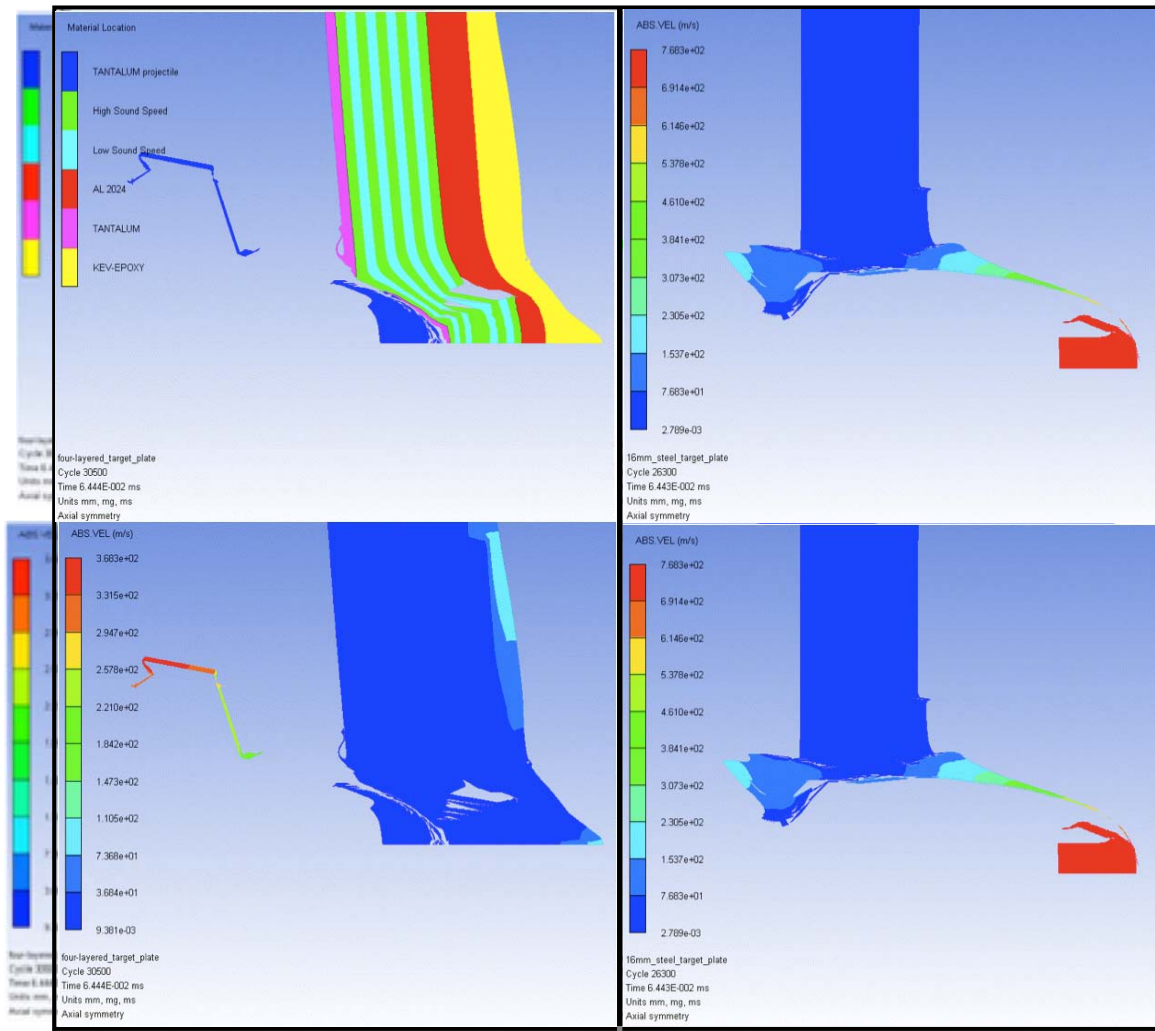
Figure 3.   Simulation by Poh (2008) to demonstrate capability of composite armor as compared to AISI 4340 steel.

In addition, Ong (2009) has conducted live firing experiments to validate this new composite armor against numerical simulations. Through this study, the composite armor was shown both experimentally and numerically to be more effective in resisting penetration than conventional high strength armor of equivalent (and slightly greater) areal density, and that the material layering sequence is fundamentally correct.

In order to reap the apparent benefits of using computers to simulate the interactions of projectile and armor systems, the description of materials and their response within the extreme terminal ballistic environment must be accurate. Although

5

the simulation mentioned above has proven the effectiveness of the multi-layered armor concept, such simulation have not been able to precisely model the actual response of the material. As pointed out by (Anderson et al., 2009), the Drucker-Prager method fails to accurately model the dynamic response of ceramics and other brittle materials. This further reinforces the need to better characterize material dynamic response in order to improve the accuracy of computational simulations, which leads to the main objective of this thesis.

3. Research Approach

The thesis will begin with an overview of shock physics and planar impact experiments before going into the experimental setup. As this is a continuation of previous research of Denzel (2010), the research will continue to focus on validating the dynamic response of ceramics as well as a new investigation into ceramet Tungsten Carbide. Several single stage light-gas gun experiments have been performed to acquire dynamic data that can better characterize the material model used for computational simulations. Finally experimental results, data analysis and final technical results will be discussed and recommendation will be made for future research.

II.   SHOCKWAVE THEORY

A good understanding of the dynamic response of materials studied under rapid impulsive loading is vital to the use of these materials in applications involving high velocity impact. Therefore there is an impetus to identify the strength properties and the inelastic deformation mechanisms of the chosen material under well-characterized, planar shockwave compression. This section describes the literature research done on the fundamentals of shock physics that will be applied to the experiments conducted for the purpose of this thesis.

A.   SHOCKWAVE FUNDAMENTALS

Strain produced in materials is directly proportional to the stress applied to it. This linear behavior only holds true up to a point at which the material will not return to its exact original shape when stress is released. This point is known as the yield point or elastic limit of the material. When a material is strained beyond its elastic limit, plastic deformation occurs. We can see how this affects material response to shock compression to high pressure by looking at some fundamental concepts.

Sound velocity is constant in the elastic region of the material and guided by the following equation:

$$C^2 = \frac{\partial P}{\partial \rho} \big|_s \tag{1}$$

This implies that in the elastic region, pressure and density are linearly related. Beyond the elastic region, P/ρ is not linearly proportional and sound speed increases with pressure or density. This nonlinearity can be observed from Figure 4.
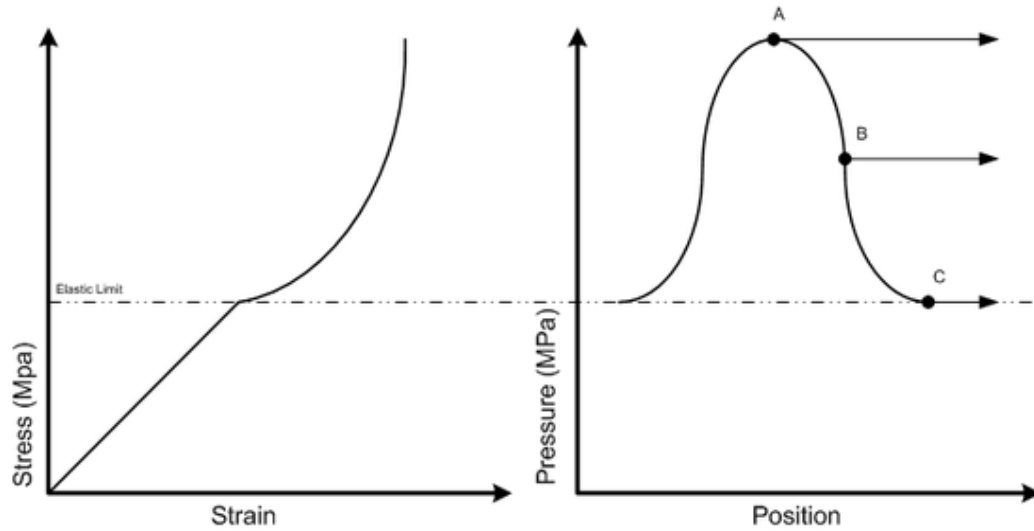
Figure 4.   Amplitude wave in regime of pressure beyond yield strength (From
Wikibooks, 2009)

Due to the nonlinearity observed, point C of the waveform will have the lowest local
wave speed while points B and A will have a higher wave velocity due to higher
pressure. This difference in velocity will eventually allow point B and A to catch up as
depicted by the time lapse diagram illustrated in Figure 5.
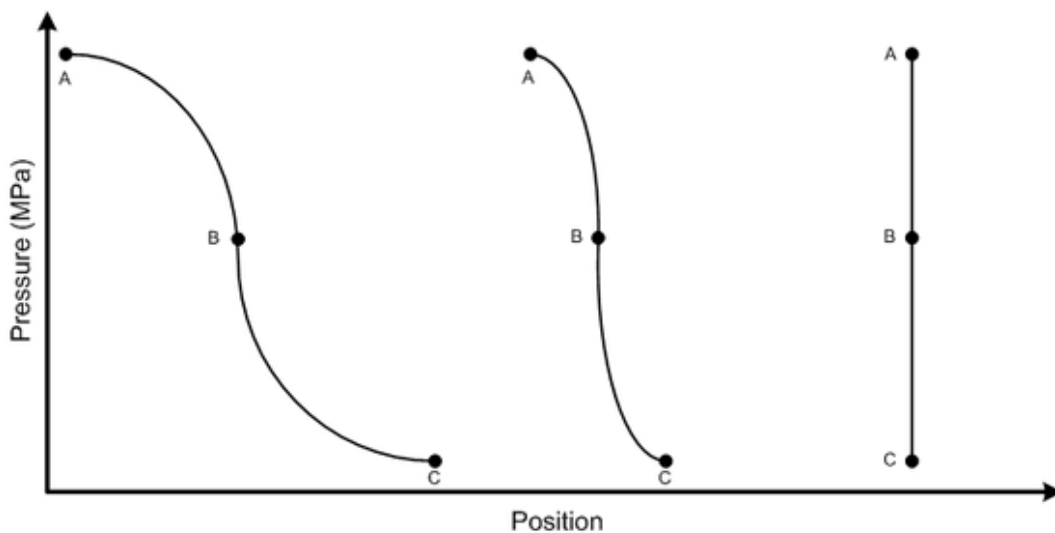
Figure 5.   Steepening of pressure wave (From Wikibooks, 2009)

With time, the pressure wave will eventually steepen at the front to form a vertical line that is known as a shockwave. This occurs because for normal materials, sound speed increases with increasing pressure.

B.   DISCONTINUITY

When a pressure wave steepens to become a shockwave, a large gradient in temperature and velocity can be observed at the front of the shock. This abrupt change from the non-shocked to the shocked stated is often taken to be a discontinuity.

On a microscopic level, large gradient in temperature and velocity at the front of the steepening wave cause an irreversible process to occur which cause entropy to increase. The net effect on a macroscopic level is that mass, momentum, and energy is conserved across the shock front, but entropy is not. Rankine, Rayleigh, and Hugoniot showed that an adiabatic shock front would violate conservation of energy, and therefore shock fronts must be non-adiabatic and irreversible (Los Alamos Science, 1985).
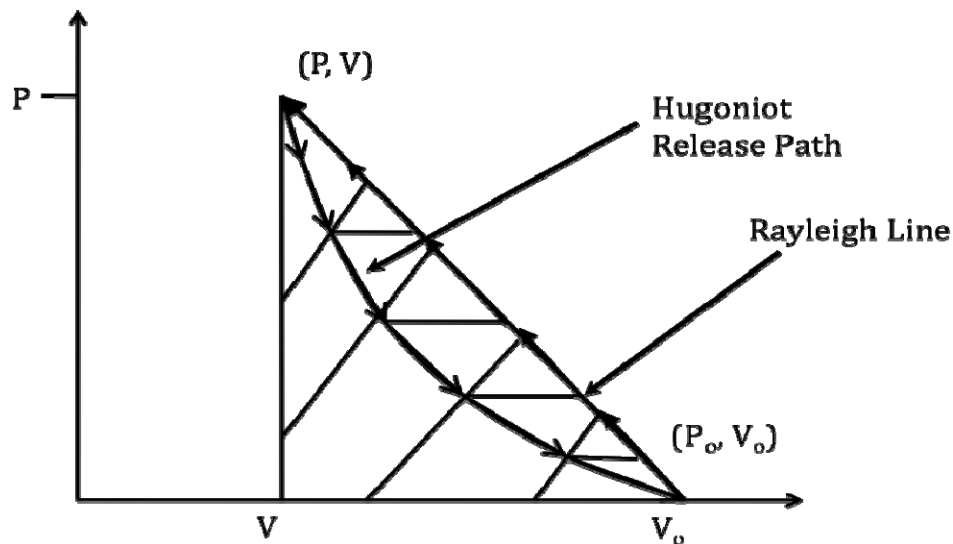
Figure 6.   Irreversible changes by shock front.

From Figure 6, we can see that the internal energy increase is proportional to the area under the Rayleigh line. If we take the release path to be close to the Hugoniot, the material will follow this curve down when pressure is released and result in some residual

energy (heat) left in the material. Therefore, it is important to note that the shock process is irreversible and the material is changed as a result of having been shock compressed. For shock loading to a very high pressure, the residual heat can be substantial.

C. RANKINE-HUGONIOT JUMP CONDITIONS

Due to reasons discussed above, the original states of particle velocity U_o, density ρ_o, internal energy E_o and pressure P_o, suddenly changes across the shock front. As mentioned above, mass, momentum, and energy are conserved across the shock front. The conservation relations do not depend upon a process path but merely upon the initial and final states of the material in question. Three equation are commonly derived from the conservation rules, and are known as "Rankine-Hugoniot Jump equations". Based on a Lagrangian coordinate system, the jump equations are expressed as shown below:

Mass: $\dfrac{\rho_0}{\rho} = 1 - \dfrac{U_p}{U_s}$ (2)

Momentum: $P - P_o = \rho_o U_s U_p$ (3)

Energy: $E - E_o = \dfrac{1}{2}(P + P_o)(V_o - V)$ Where $V = 1/\rho$ (4)

With 3 equation and 5 unknowns (e.g., U_S, U_P, P, and E), it becomes clear that another relationship is required to relate some of the states. This equation is often referred to as Equation of state (EOS). Unfortunately, there exists no EOS's that can be derived from first principles to describe non-linear elastic materials. This drives us to measure two of the five unknown quantities experimentally. This in turn allows us to define an EOS.

D. SHOCK HUGONIOT IN U_S – U_P PLANE

In the past, many experiments were conducted to determine EOS's for many materials, and it was found that shock and particle velocity are linearly related in most materials by the equation shown below:

$U_s = C_o + SU_p$

(5)

Therefore if U_s and U_p are determined experimentally at a number of different shock states for a certain material, the shock Hugoniot in $U_s - U_p$ plane can then be easily described. When the data points are plotted in the $U_s - U_p$ plane, doing a linear fit through the points would give the constant C_o at the y-axis intercept, and also determine the slope. The bulk sound speed C_B is typically a very good approximation for this constant C_o. Figure 7 illustrates an example of a $U_s - U_p$ Hugoniot plot for Tungsten Carbide.
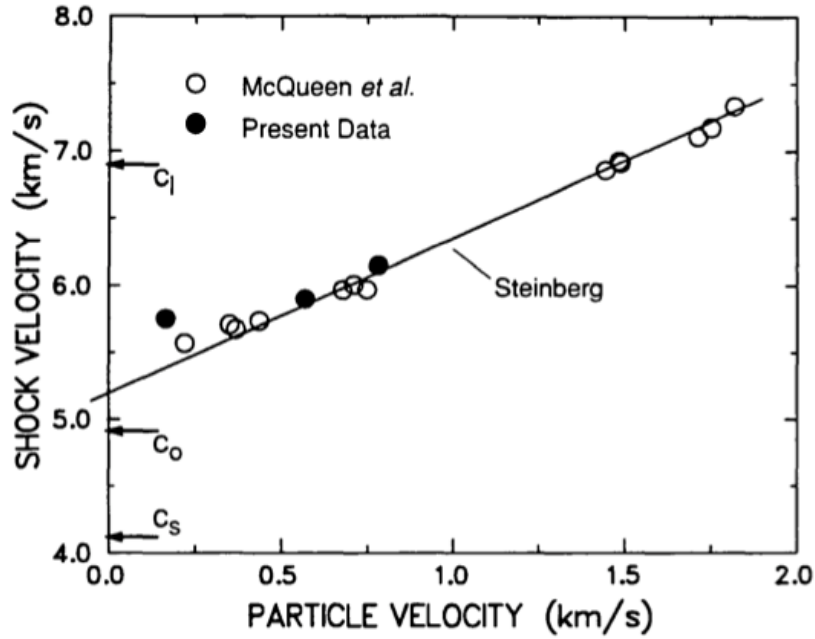
Figure 7.   Hugoniot lot in $U_S - U_P$ of tungsten carbide (From Grady, 1995)

Hence, an EOS-derived Hugoniot can then be determined from experimental data. The acquisition of these experimental data is exactly the main focus of this thesis research in order to fully describe the shock states.

E.   PLANAR IMPACT EXPERIMENTS

Light-gas guns are commonly used to launch flat-plate impactors onto flat plate targets to produce normal shocks into the targets. These normal shocks are critical to produce the uni-axial strain conditions required to use the simple theories described

11

above and thus obtain EOS information from simple particle velocity and shock speed measurements. This method offers tight control over the stress-time history of the sample. Principle diagnostics are the Laser Velocity Interferometer for Any Reflector (VISAR), and time of arrival pins.

The experiment usually involves a projectile impacting a stationary target plate at the velocity of U_D. A discontinuity of particle velocity and stress between the target and projectile will be formed on impact, and shockwaves are immediately developed to relieve this discontinuity. The developed shockwaves will then propagate away from the plane of impact in both the projectile and target. With the help of the VISAR system and PZT pins, the velocity of the shockwave can then be determined. Projectile velocities U_D is measured by shorting 6 electrically-charged pins located at measured distances (millimeters ahead of the target sample) and subsequently particle velocity U_P can be either measured with the VISAR system or determined using the jump conditions. These parameters, together with the help of fundamental equations will allow us to develop an EOS under dynamic loading conditions.

As mentioned above, to determine the fundamental shock response of a target material, a plot of shock wave velocity U_s versus particle velocity U_p is required. Therefore several impact experiments at various U_D will have to be conducted.

III.   EXPERIMENTAL METHODS

The measurement of dynamic properties of materials requires the use of well-developed experimental techniques and often sophisticated equipment to obtain satisfactory data. In this section of the thesis, equipment used and theory behind how the experiment is conducted to acquire the data will be elaborated.

A.   LIGHT-GAS GUN
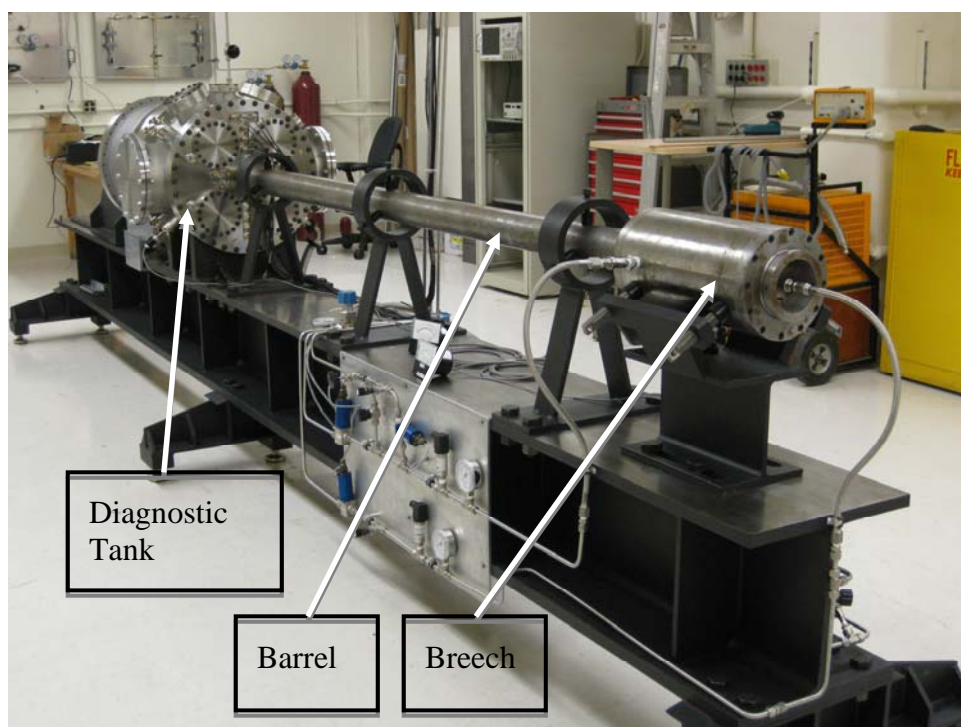
Figure 8.   NPS light-gas gun assembly

All the experiments conducted for this thesis was done on a 76 mm bore single stage light gas gun housed in the impact physic lab of the Naval Postgraduate school (NPS) as shown in Figure 8. This helium-driven gas gun was designed to accelerate projectiles up to velocities below 0.5 km/s, thus creating high-pressure states that can be used to characterize the fundamental dynamic responses of the material tested. The breech utilizes a "wrap around" design that eliminates the need of any diaphragms.

High-pressure helium gas contained in the breech is separated from the launch tube with the use of o-rings installed on both ends of the projectile. Figure 9 shows the picture of the projectile and the breech:
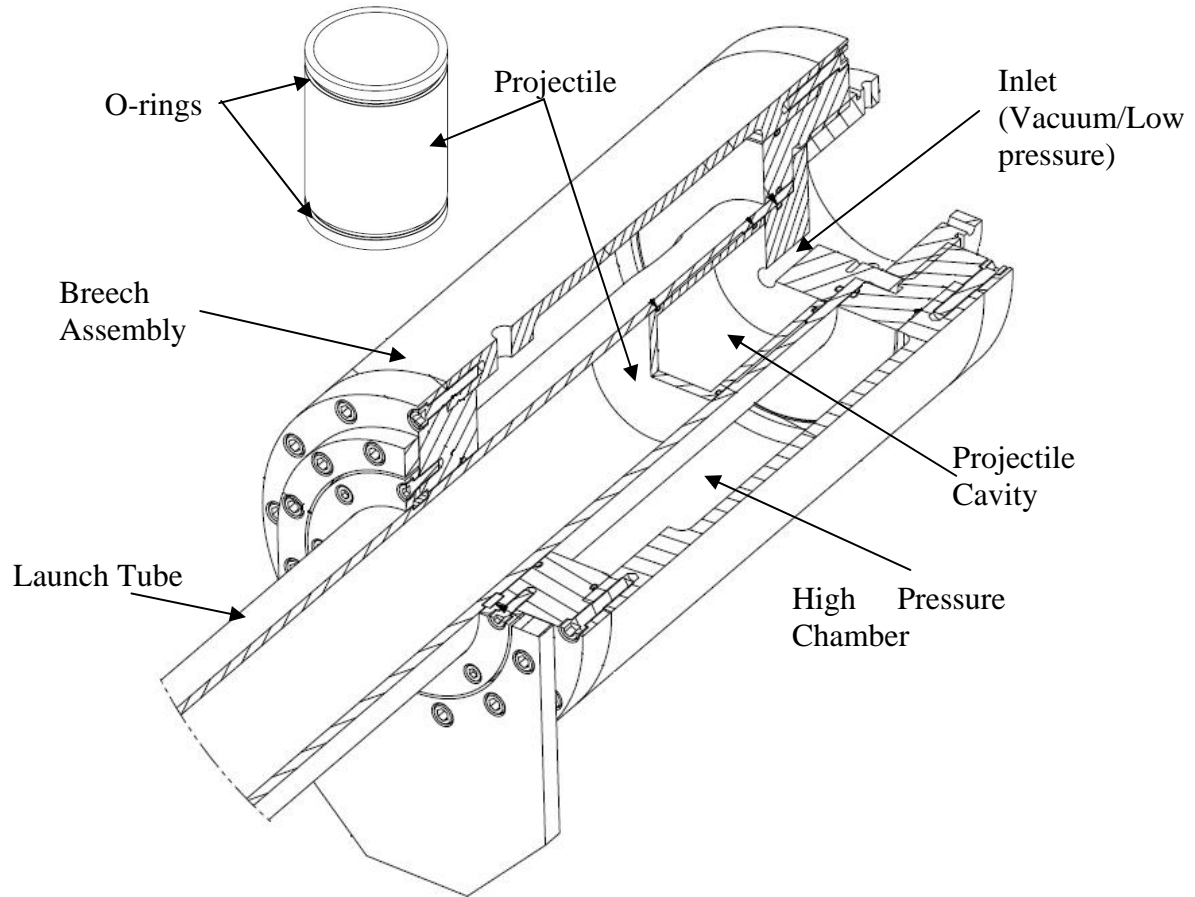
Figure 9.   Breech assembly and projectile of gas gun (From Ho, 2009)

The projectile is launched when a small amount of low-pressure is introduced behind the projectile, pushing it past the ports of the breech and thus allowing the high-pressure helium gas to accelerate the projectile.

To ensure that the launch tube is properly aligned to the target, adjustments were regularly made to the launch tube support assembly with the help of a class 3b He:Ne laser sent down the entire length of the launch tube and retro-reflected back. In order to

ensure a very flat impact condition, the alignment of the launch tube must be less than 1 mrad relative to the target plane. The alignment of the barrel is adjusted as shown in Figure 10.
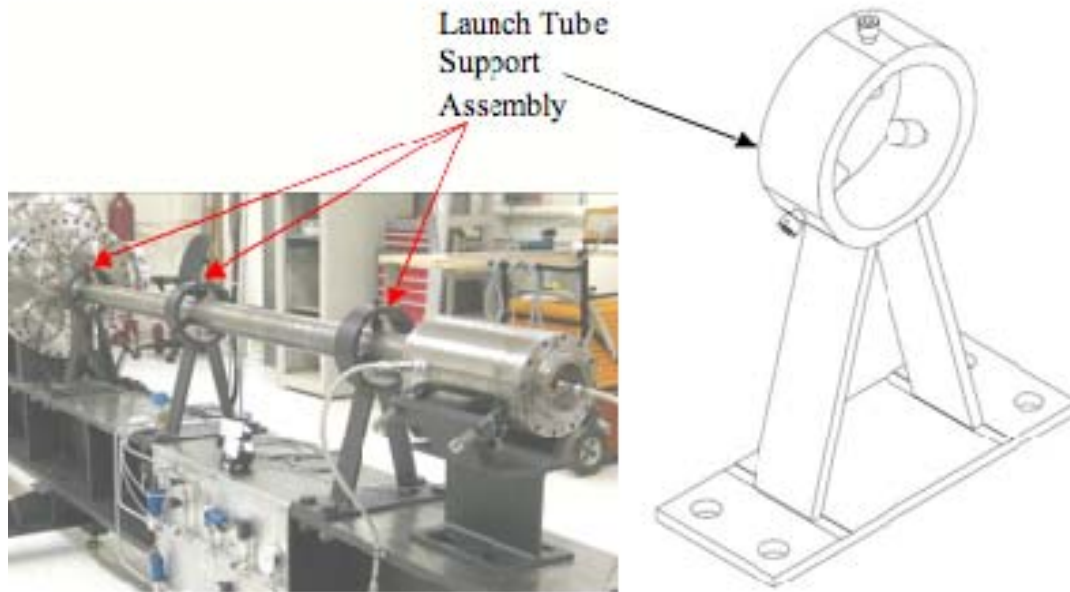
Figure 10.   Figure of launch tube support assembly (From Ho, 2009)

Finally the projectile will impact onto the target, that is mounted in diagnostic tank assembly. The effect of air buildup between the target and projectile is minimized by creating a vacuum condition of <30 millitorr in the barrel and the diagnostic tank assembly prior to firing. An expansion chamber between the end of the launch tube and target assembly is provided to further ensure that the air buildup is kept to a minimum.

Lastly, the catcher tank assembly ensures that after impact, momentum of the debris is stopped to minimize damage to the gun. This is achieved with several layers for energy absorbing material in the form of aluminum honeycomb sheets, a blast shield—an extra layer of mild steel to prevent any debris from striking the rear surface of the catch tank and a sliding baffle to absorb energy. The baffle has nylon wheels and is a sealed cylinder of steel. To ensure that the honeycomb can be uniformly compressed, a thick

aluminum place is placed in front of the honeycomb so that on impact, the plate compresses the honeycomb material relatively uniformly causing energy to be dissipated. Figure 11 shows the catcher tank assembly.
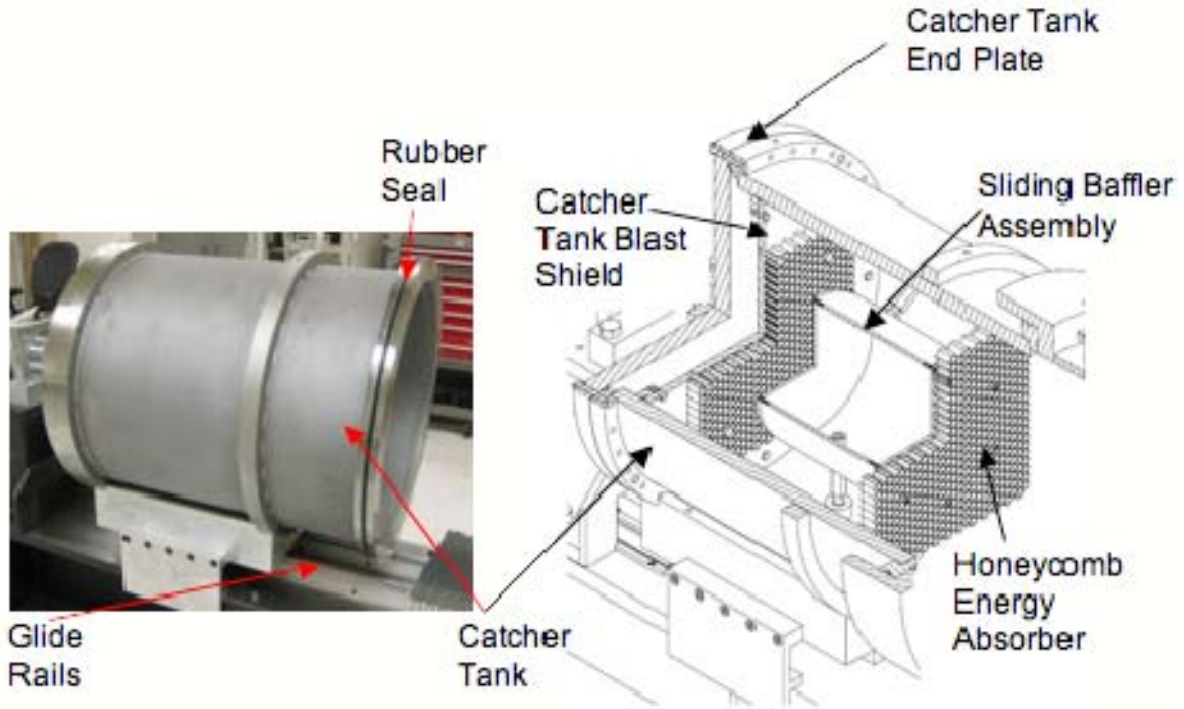
Figure 11.   Catcher tank assembly (From Ho, 2009)

B.   SAMPLE CHARACTERIZATION

In order to make accurate dynamic property measurements, we must first characterize certain initial properties for the selected material to be experimented. This initial characterization is important to establish the baseline properties for the material being studied and later to be used for the accurate derivation of dynamic loading properties of the material. Especially for sintered materials like polycrystalline ceramics, it must be ensured that it is close to being isotropic. As shown by Gust and Royce (1971), previous experimental results for similar materials have clearly shown that initial sound speed depends strongly upon initial density and that even small deviations in initial density cause measurable difference in initial sound speed and dynamic properties.

16
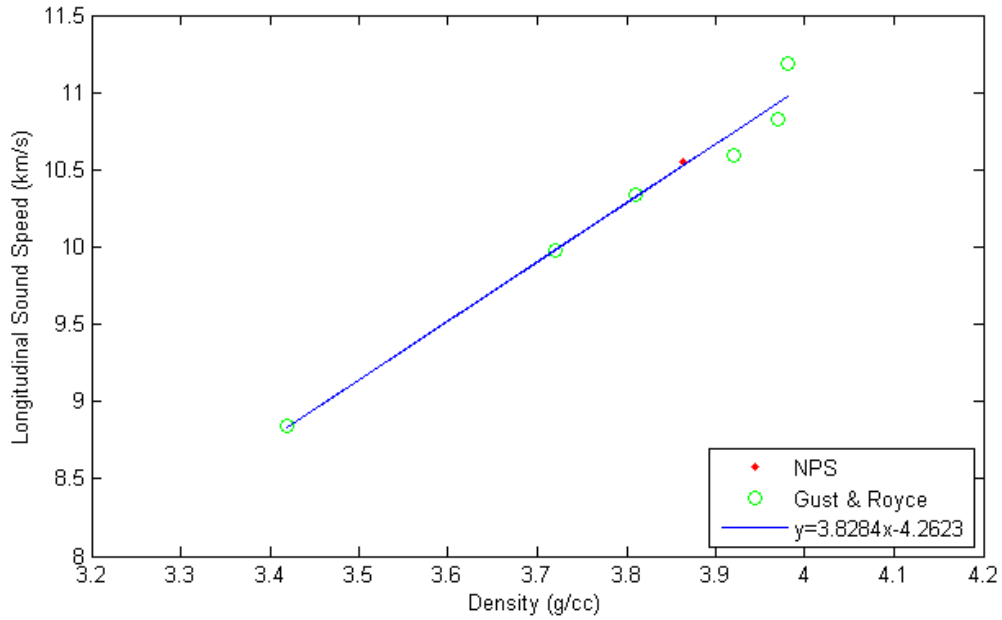
Figure 12.   Longitudinal sound speed vs. density of ceramics (From Denzel, 2010).

From the plot in Figure 12, it can be seen that the measured density and longitudinal sound speed of the Corbit-98 is in agreement with the previous work of Gust and Royce (1971).

1.   Initial Density

As mentioned in Denzel (2010), the initial density of the Corbit-98 sample used in the experiments of this thesis was measured at Los Alamos National Laboratory (LANL) using standard immersion technique that is based on Archimedes principle. The sample's weight is measured in dry air and submerged in water. By knowing the exact temperature of the distilled water, one can obtain the volume displaced by the sample by dividing the difference in weight between the dry and the underwater measurements by the water density.   Then, knowing the samples mass and volume, once can very accurately calculate its density. The density was found to be $\rho_o = 3.864 \pm 0.005$ g/cc.

Density of the Ceramat Tungsten Carbide samples was determined by using a mircometer to measure diameter and thickness and an electronic scale with an accuracy

of ± 0.1 gram to measure their weight. This is possible due to the high tolerance for the samples as supplied by General Carbide, the density was found to be 14.03 g/cm^3 for samples marked GC-915 and 12.82 g/cm^3 for samples marked GC-330, which coincide with the figures published on the General Carbide's specification sheet for the material.

2. Elastic Sound Speeds

Using Hooke's law along with Newton's Second Law, one can show that the speed of sound within a material is a function of the innate properties of the material. The general relationship between the sound speed in a solid, density and elastic constants is shown by the following general equation:

$$C_i = \sqrt{\frac{M_{ij}}{\rho}} \tag{6}$$

where C$_i$ is the sound speed, M is the appropriate elastic constant and ρ is the material density. It must be noted that the subscript ij of the elastic constant M is used to indicate the wave type being considered. Types of possible sound wave include longitudinal sound speed (C$_L$), shear sound speed (C$_S$), bulk sound speed (C$_B$):

Bulk Sound Speed: $$C_B = \sqrt{C_L^2 - \frac{4}{3}C_s^2}; \tag{7}$$

From these sound speeds, modulii and Poisson ration can then be determined:

Longitudinal Modulus: $\quad\quad\quad\quad\quad\quad F = \rho_o C_L^2; \tag{8}$

Shear Modulus: $\quad\quad\quad\quad\quad\quad\quad G = \rho_o C_S^2; \tag{9}$

Bulk Modulus: $\quad\quad\quad\quad\quad\quad\quad K = \rho_o C_B^2; \tag{10}$

Poisson Ratio: $\quad\quad v = \dfrac{(3K - F)}{(3K + F)} = \dfrac{(F - 2G)}{2(F - G)} = \dfrac{(3K - 2G)}{2(3K + G)}; \tag{11}$

Both C$_L$ and C$_S$ of the sample used for the purpose of this thesis were measured using a commercially available ultrasonic pulse-echo system made by Panametrics Inc. (a division of Olympus). This system consists of a pulse unit that can be used with either longitudinal or shear transducers, in pulse-echo geometry. The observation and measurement of timing between pulses were done using a fast digital oscilloscope. More than 1 sample of each material was measured to ensure that the samples were of uniform

quality. For each sample, many reflections were measured and a least square's fit was used to obtain the sound speeds. Table 1 summarizes the acoustic properties measured and calculated for both ceramic Corbit-98 and ceramet tungsten carbide:

Table 1.   Properties of target sample

Properties	Corbit 98	WC/Co GC-330	WC/Co GC-915
Density (g/cm^3)	3.864	12.82	14.03
Elastic Wave Velocities (km/s)			
Longitudinal	10.55	6.29	6.67
Shear	6.18	3.63	3.92
Bulk	7.77	4.69	4.90
Shear Modulus (GPa)	148	169	216
Longitudinal Modulus (GPa)	430	507	624
Bulk Modulus (GPa)	233	282	337
Poisson Ratio	0.239	0.250	0.236

C.   HUGONIOT MEASUREMENT EXPERIMENTS

As mentioned earlier, one of the main objectives of this thesis is to perform impact experiments to measure shock and particle velocity over a range of impact in order to determine the Hugoniot-EOS for the material studied. In this section, the theory and physical set up of the gas gun planar impact experiment will be explained in detail.

1. Flyer Velocity
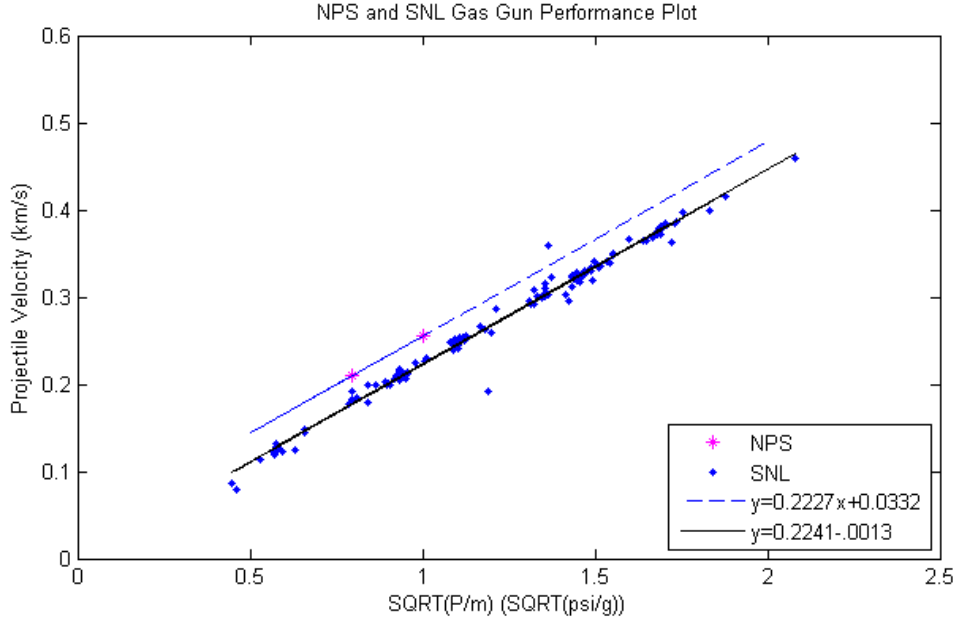
Figure 13.   Gas gun performance plot

By design, the gas gun achieves desired projectile speed by adjusting the breech pressure based on the projectile weight. This calculation is based on the gun performance curve shown in Figure 13. After the projectile is fired, its velocity before impact is accurately determined by using a stepped circular array of electrical shorting pins mounted on the target plate. The main purpose for accurately measuring this velocity is to derive the particle velocity in the target, which will be elaborated on later in this section.

2. Shock Speed U_s

For material under elastic compression, the wave speed must be close to the longitudinal sound speed. However for finite amplitude waves where shock-up is expected, shock velocities will be greater than C_B. For these kinds of planar experiments,

shock speed U_S is actually not directly measured. It is in fact, derived by dividing the thickness of the target and the shock transit time as shown by the equation:

$$U_s = \frac{x}{t}$$

Shock transit time is known by measuring the time from impact until the breakout of the first wave at the back of the target. To be able to measure this short transit time (on the order of a microsecond), time must be resolved down to nanoseconds. This is achieved through the use of piezoelectric (PZT) pins and interferometers.
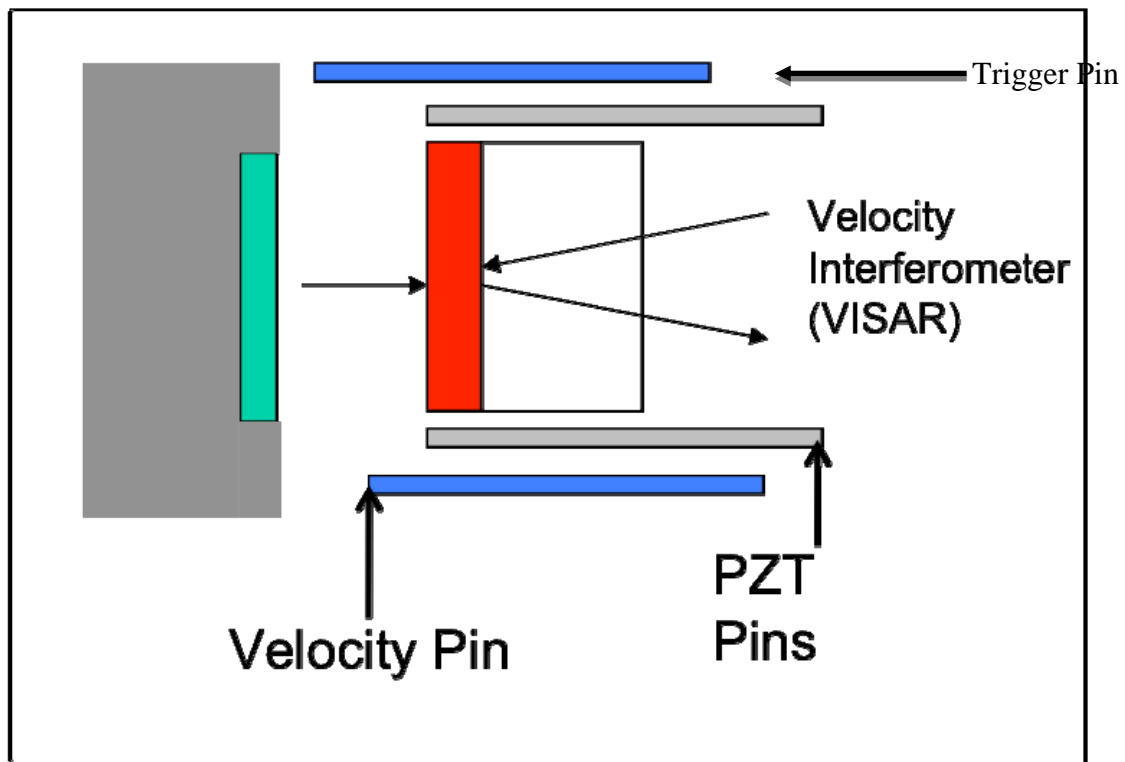
Figure 14.   Schematic of planar impact setup

From the diagram shown in Figure 14, it can be seen that a trigger pin is affixed to the target so as to trigger the electronic system upon impact of the projectile. A Velocity Interferometer System for Any Reflector (VISAR) on the other end of the target is used to measure the time at which the first breakout of the shockwave appears. Additional PZT pins allow projectile impact time to be measured. As some materials are not

21

reflective enough to allow direct interface with the VISAR, a very thin foil may be applied with epoxy to the target to increase reflectivity. Finally, impact velocities were measured by shorting electrically-charge velocity pins located at measured distances a few millimeters ahead of the target sample.

3. Particle Velocity

For planar impact experiments, particle velocity is closely related to flyer velocity. For symmetrical impact, where both the flyer and target are of the same material, the math is greatly simplified and the particle velocity can be taken as $0.5*U_D$ or half the flyer velocity.

For the unsymmetrical impact experiment, to get U_{p2} or particle velocity in the target, we use the fact that across the impact interface, pressure and particle velocity must be conserved as shown in Figure 15.
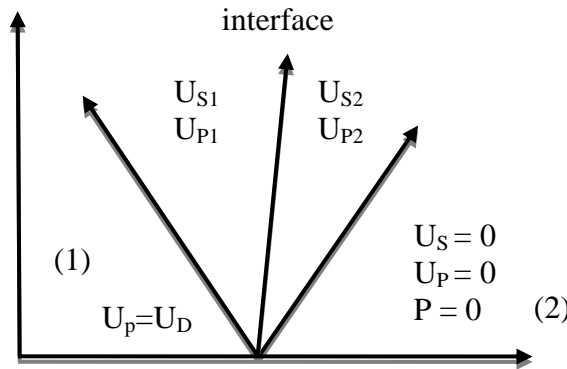
Figure 15.   x-t diagram for unsymmetrical impact

Usually for the an unsymmetrical impact experiment, Hugoniot of flyer is known but flyer velocity and shock velocity in the target are required to be measured.

For the flyer (material 1), in general we have:

$$U_{S1} = S_1 U_{p1} + C_1 \tag{12}$$

$$\Rightarrow P_1 = \rho_{01}(S_1 U_{p1} + C_1) U_{p1} \tag{13}$$

Since $U_{p1} = U_D - U_{p2}$, we can rewrite Equation (13) as:

22

$$P_1 = \rho_{01}(S_1(U_D - U_{P2}) + C_1)(U_D - U_{P2})$$
$$\Rightarrow P_1 = (\rho_{01}S_1)U_D^2 - 2\rho_{01}S_1U_DU_{p2}^2 + \rho_{01}S_1U_{P2}^2 + \rho_{01}C_1U_D - \rho_{01}C_1U_{P2}$$

$$\Rightarrow P_1 = (\rho_{01}S_1)U_{p2}^2 - (2\rho_{01}S_1U_D + \rho_{01}C_1)U_{P2} + \rho_{01}(S_1U_D^2 + C_1U_D) \tag{14}$$

Since U_s can be derived from the experiment, pressure P_2 can then be determined by the following equation:

$$P_2 = \rho_0 U_{S2}U_{p2} \tag{15}$$

Since pressure P_1 and P_2 must be equal (from conservation of mass and momentum), we obtain

$$(\rho_{01}S_1)U_{p2}^2 - (2\rho_{01}S_1U_D + \rho_{01}C_1)U_{P2} + \rho_{01}(S_1U_D^2 + C_1U_D) = \rho_{02}U_{S2}U_{p2}$$

$$(\rho_{01}S_1)U_{p2}^2 - (2\rho_{01}S_1U_D + \rho_{01}C_1 + \rho_{02}U_{S2})U_{P2} + \rho_{01}(S_1U_D^2 + C_1U_D) = 0 \tag{16}$$

From Equation (16), U_{p2} can then be found.

D.   HUGONIOT ELASTIC LIMIT

In addition to establishing a point on the shock Hugoniot U_S - U_p plane, an important objective of this thesis is to determine the dynamic yield point or the Hugoniot Elastic Limit (HEL) σ_{HEL} for the materials studied.
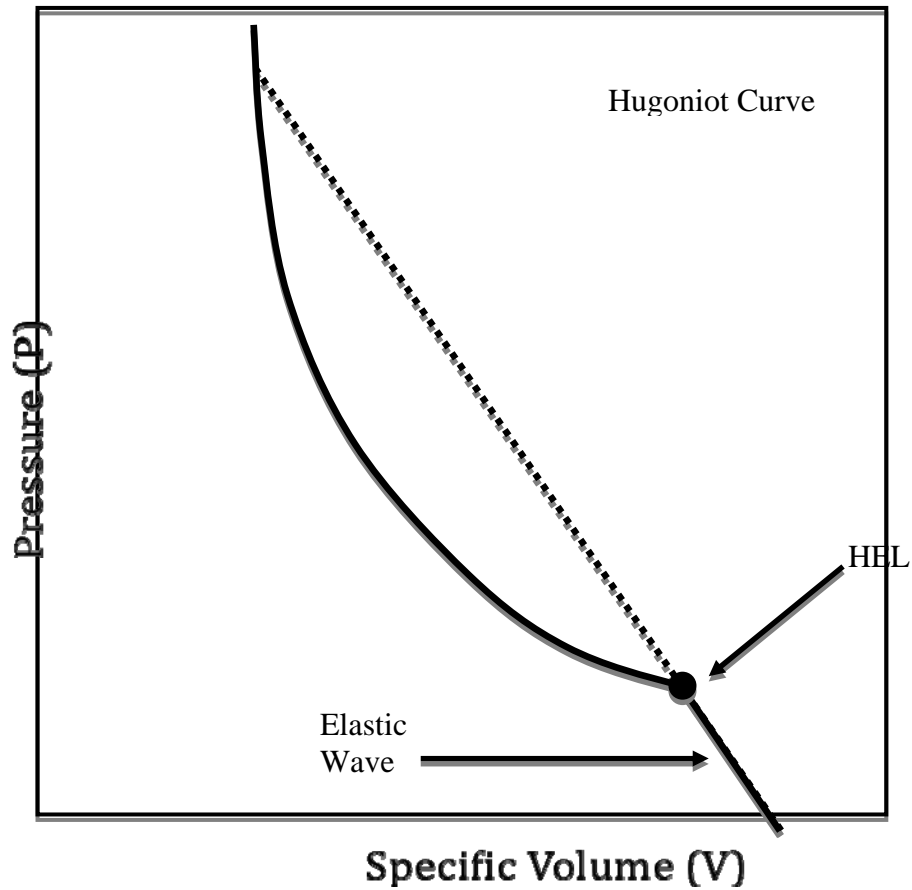
Figure 16.   Shock Hugoniot in P-V plane for a material with strength

From Figure 16, the HEL point is shown at the end of the slope of the elastic wave, as an inflection point. Below the HEL would be the elastic region and above, the plastic region. In the elastic region, the velocity of the wave would be the longitudinal sound speed C_L. In the plastic region, the slope of the Raleigh line would be less than that of the elastic Hugoniont for low stresses, and this results in a shock velocity below C_L. For high stresses the shock speed can be greater than the longitudinal sound speed.
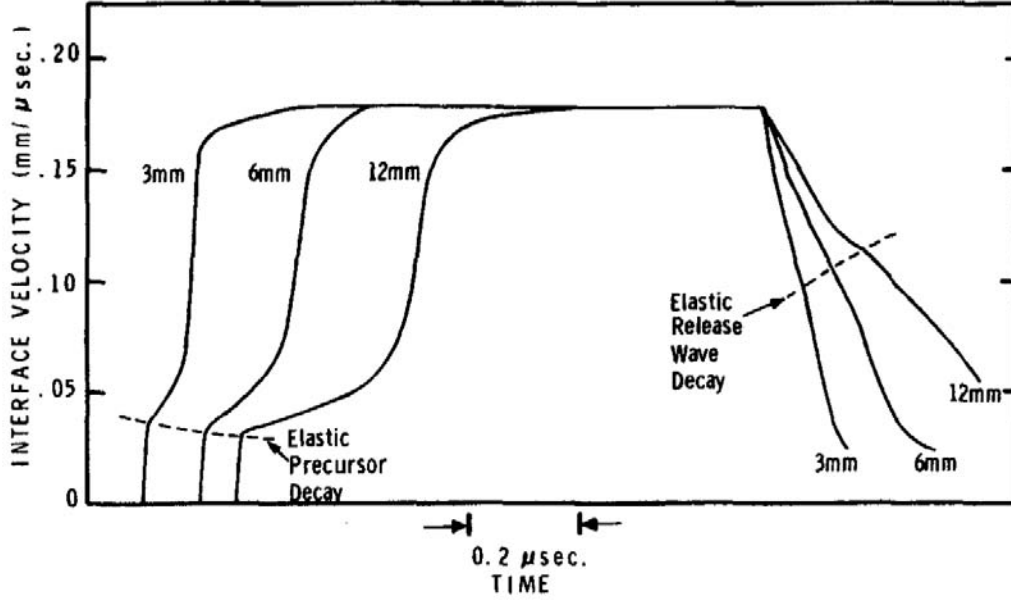
Figure 17.   A typical wave profile of a free-surface VISAR measurement of aluminum
(From Isbell, 2005)

Due to the different sound speeds in these regions, a cusp can easily be observed in the wave profile when the material is stricken up to the plastic region as illustrated in Figure 17. Therefore, in order to determine σ_{HEL}, first of all the amplitude of the wave at the cusp is measured while taking note that it's the free surface velocity. Since the wave would be travelling at the longitudinal sound speed C_L at the yield point, and the initial density of the material can be measured, σ_{HEL} can then be derived by applying the momentum jump condition:

$$\sigma_{HEL} = \rho_o U_S U_P = \rho_o U_S * (\frac{1}{2} U_{fs}) \tag{17}$$

For an elastic wave, U_S is simply C_L and hence,

$$\sigma_{HEL} = \frac{1}{2}(\rho_o C_L U_{fs}^E) \tag{18}$$

The above equation is only applicable to a free surface experiment where no window was used.

E.   SPALL MEASUREMENTS

Another objective of this thesis is to measure the spall strength of the materials studied. Spall fracture is usually a result of the interaction of compressive stress wave from relatively low-impedance interfaces (normally free surfaces) and subsequent wave interactions as shown in Figure 18. The release wave interactions cause tension to be generated in the target.
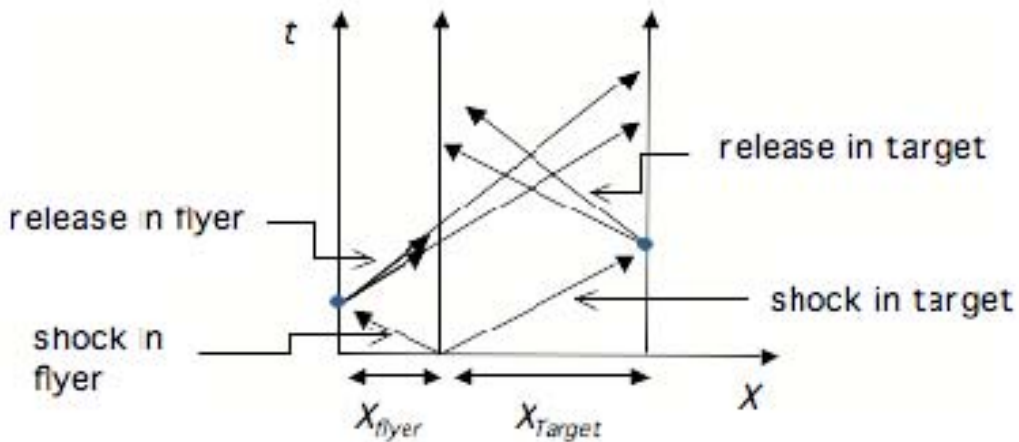
Figure 18.   Interaction of release wave

The spall fracture data in this thesis were obtained by planar impact experiments where uniaxial strain conditions exist. Such an impact experiment is usually designed to allow two release waves interact in the target and thus bringing the material into tension dynamically. If the tension exceeds the spall strength of the target, the target will fail and part at this plane. In the design of the experiment, the thickness of the target and impactor are chosen in such a way that allows the release wave from both free surfaces to meet at approximately at the center of the target.
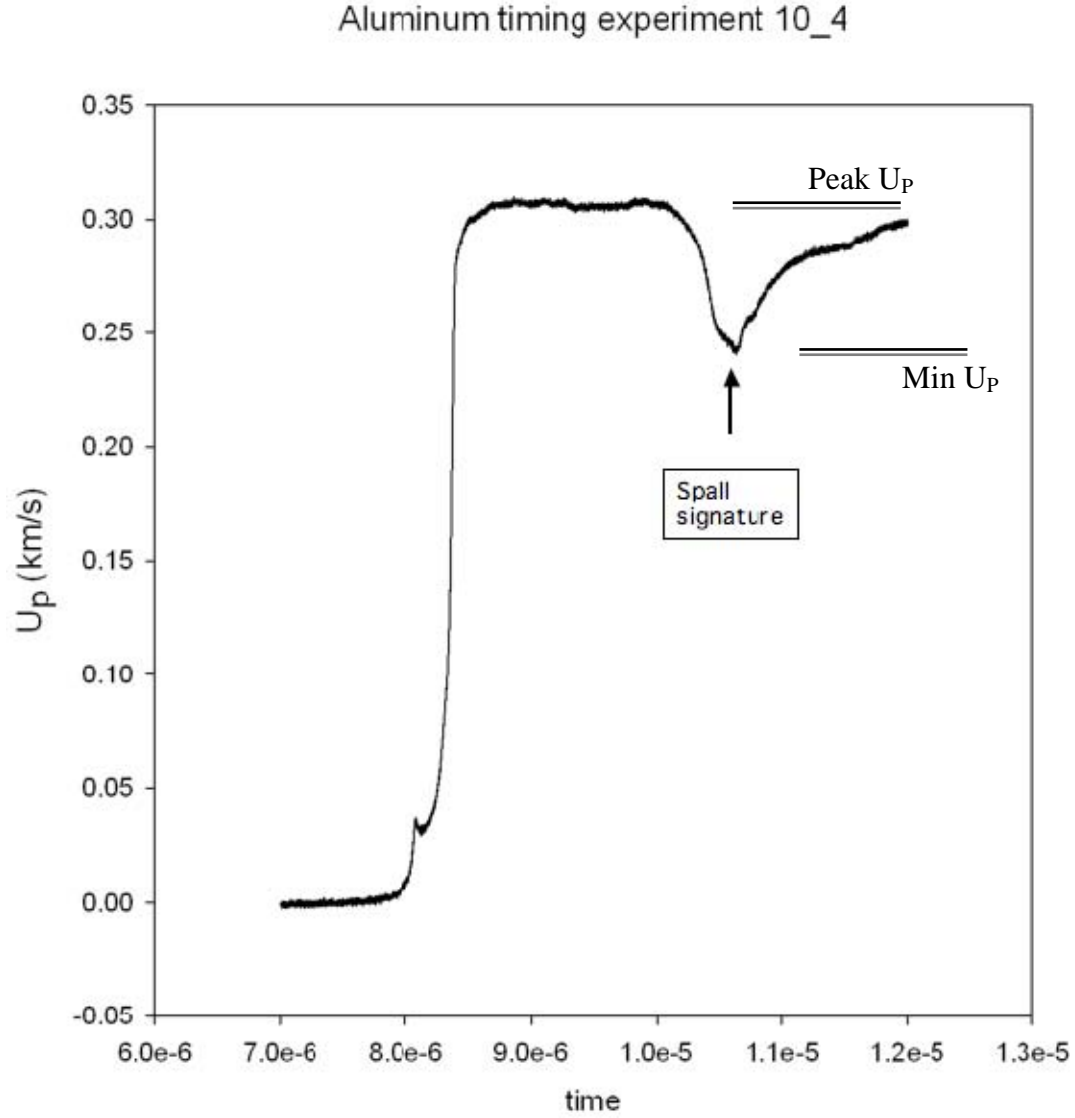
Figure 19.   A typical free surface VISAR wave profile showing a spall signature (From Denzel, 2010)

Figure 19 shows a typical wave profile of a free surface planar impact experiment exhibiting a spall signature. The simplest but also a least accurate way to estimate the spall strength is to find the difference in peak particle velocity and minimum particle velocity. Then applying the momentum jump condition yields the following equation:

$$\sigma_{spall} = \frac{1}{2}\rho_o U_x \Delta U_P \tag{19}$$

The wave speed U_x used in a ductile material shocked above HEL is the bulk sound speed (C_B). As for brittle materials like ceramics, spall strength cannot be accurately determined with the use of bulk sound speed as the wave speed in the above equation. However, for simplification and for just an estimation of spall strength, bulk sound speed is knowingly used to acquire an approximate value of the spall strength.

F. TARGET SETUP

1. Target Holding Plate

The most generic target holding plate used for the purpose of this research is a six-inch diameter aluminum 6061 disc as shown in Figure 20:
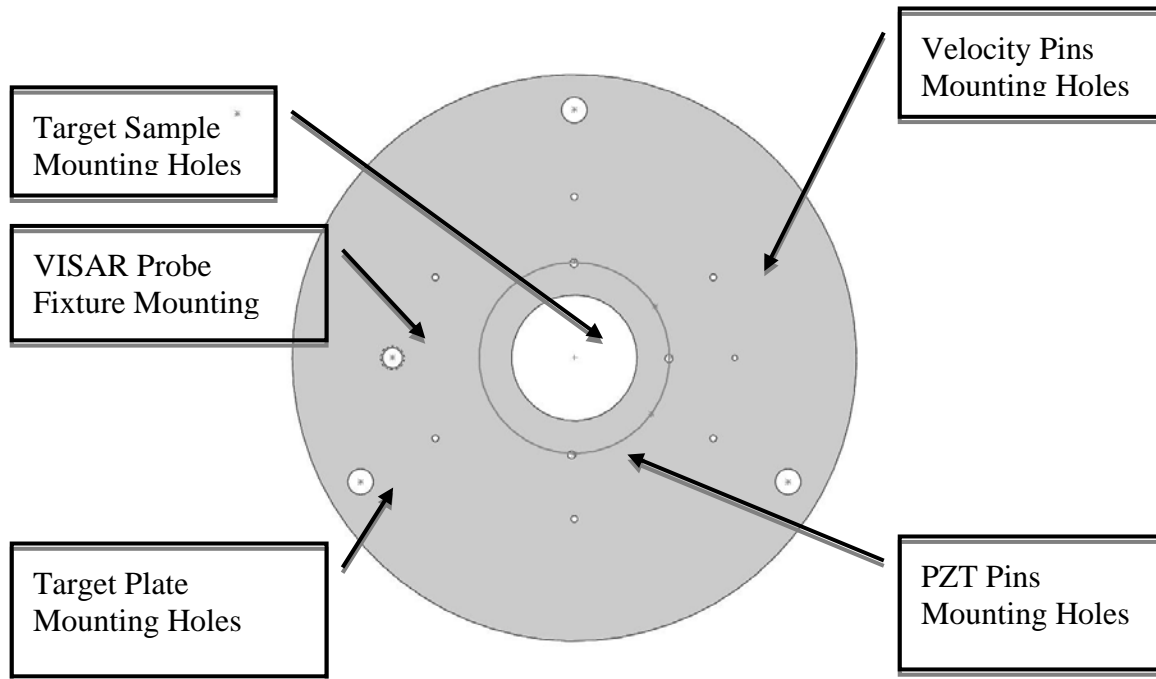
Figure 20.   Schematic of target holding plate

VISAR, PZT and velocity pin diagnostics were utilized for the purpose of this research. From Figure 20, it can be noted that the target holding plate has a total of 7 holes for velocity pins (1 being the grounding pin), 3 holes for PZT pins, one for the mounting of the VISAR probe and 3 for mounting of the plate on to the diagnostic tank.

28

Before mounting any of the diagnostics and target material, the plate is first lapped on a fine sand paper on a granite flat to a surface finish of 12 microns. Similarly, the target sample must be lapped to be flat and parrallel.

2.   Projectile
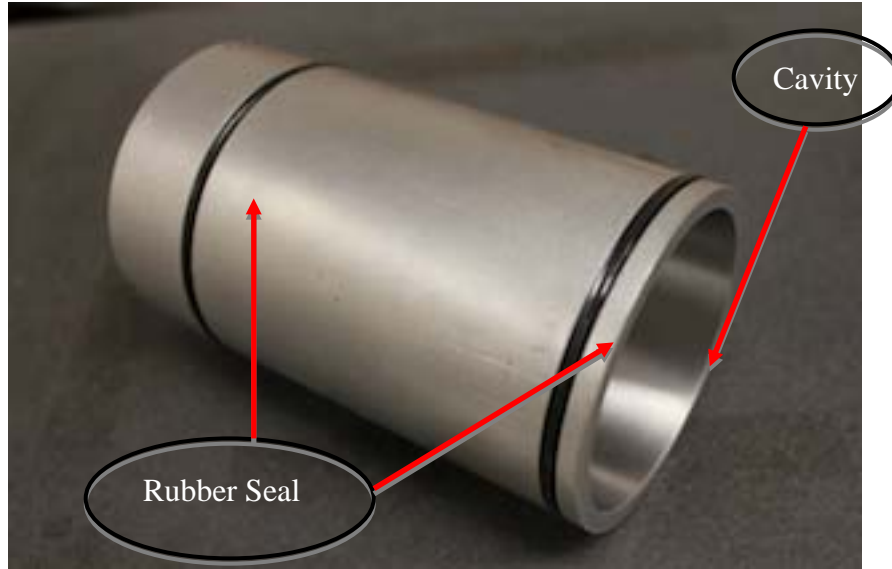
Figure 21.   Aluminum alloy 6061 projectile

The generic projectile as shown in Figure 21 is used for all the experiments conducted. The projectile is made of aluminum alloy 6061 and machined to a tolerance of less than one thousands of an inch on the outer diameter as well as on the impacting face.

3.   VISAR

The laser velocity interferometer measures surface or interface velocity as a function of time. Either free surface motion or motion of the interface between the target sample and a transparent window material can be determined with great time and velocity resolution. The type of interferometer used for the purpose of this thesis is a velocity interferometer for any reflector. VISAR is a modified Michelson interferometer where velocity instead of displacement are directly obtained. This state of the art VISAR

system was acquired from National Security Technologies (NSTEC). With a small physical footprint and ease of use, this system makes it perfect for research conducted by students. The laser utilized for this system is a class 4 frequency doubled Nd:YAG solid state continuous wave (CW) laser. Procured from Coherent, this laser is designed to operate in the wavelength of 532 nm. The delivery system for the laser to the diagnostic tank is an optical-fiber system that is safe and effective method for coupling the laser light into the target chamber. The output of the laser is focused into this 50 μm step index optical fiber through voltage controlled wave plates (Pockels cell). An optical fiber probe is connected at the end of this optical-fiber system through a vacuum flange in the diagnostic tank. The laser light is projected onto the target through a Plano-convex lens affixed at the tip of the probe, and this same lens serves to collect the reflected light. The reflected laser light is then sent back to the interferometer cavity and interference occurs. Quadrature signals that contain information about the interference pattern are routed to four 928 photomultipliers before the converted electrical signals are sent to a Tektronix DPO4104 transient recorder. The recorded data is then finally stored on a connected laptop ready for analysis.

4.   Velocity Pins

As mentioned earlier in this section, there's a need to measure the projectile velocity and this is achieved with a stepped circular array of electrical shorting pins as shown in Figure 22. The use of these pins allows the speed as well as the angle of tilt of the projectile to be measured. A total of seven pins are used for every experiment conducted for the purpose of this thesis. Six of the pins are aligned at 60 degrees apart from each other in a circular array. The 7th pin or the ground pin is placed in such a way that it will be the first to be impacted. Every pin is individually shrink-wrapped so as to be electrically isolated from the target holding plate till the impact of the projectile occurs. The non-impact side of the pins are soldered to a wirings harness that is connected to a pin circuit. This pin circuit generates an electrical pulse for each pin that

is shorted on impact by the projectile. Using a least-squares fit to the times at which the pins were shorted, combined with the various lengths and angles, both projectile velocity and tilt can then be derived.
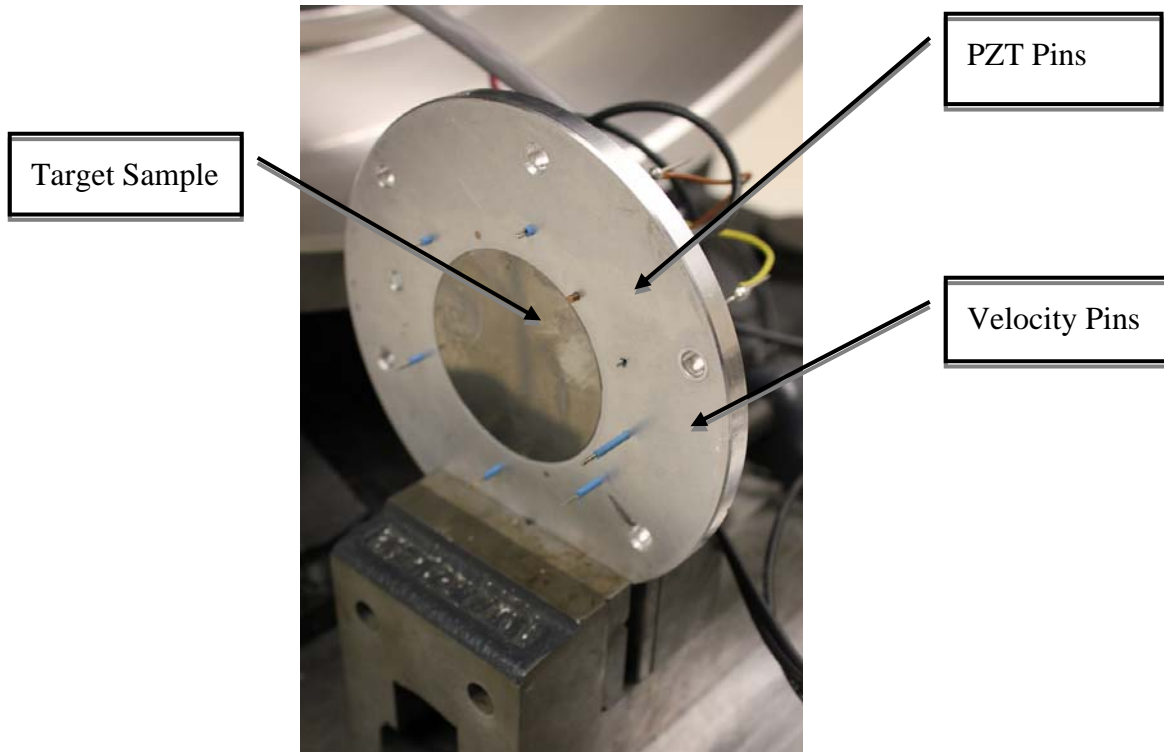
Figure 22.   Target holding plate with pins and target sample mounted.

5.   Piezoelectric (PZT) Pins

In order to determine the time of impact, PZT pins are used. The PZT pins are placed 180 degree apart on a diameter of the target plate holder and are set flush with the impact surface. The non-impact side of the pins is connected directly to the diagnostic system through a 50Ω coaxial cables. A separate PZT pin is used as the trigger pin for activating the VISAR system as well as the data recording instrumentation.

6. Details of Sample Preparation

a. *Ceramic Corbit-98*

In order to prepare a Corbit target, first the supplied square plate (50 mm by 50 mm) as received from the manufacturer is cut to fit in the round hole of the target holding plate using a diamond hole saw. Due to the fact that ceramic is both a super hard and brittle material, the cutting process is a delicate and time-consuming process. In order to ensure that the brittle samples do not crack towards the end when the saw is almost through, a sacrificial piece of ceramic is glued to the bottom. To prevent the sample and the saw bit from being overheated due to the long cutting process, the ceramic sample must be immersed in a basin of coolant.

After the ceramic sample has been cut, it is then lapped on a rotating wheel affixed with a micro cloth which is coated with 9 μm diamond suspension solution, followed by a 6μm diamond solution to achieve the required surface finish. The ceramic sample is then polished on a diamond impregnated lapping plate acquired from UHL Technologies, and is designated DIABLAP. The sample is typically lapped to a flatness of 10 μm. An example of rotating wheel used for lapping of the target sample is shown in Figure 23.

Figure 23.   Buhler rotating wheel used for lapping of samples.

Depending on the type of experiment conducted, a thin sheet of reflective foil, such as a stainless steel shim of less than 5 μm in thickness may be glued to the back of the target sample for the purpose of improving the reflection of the VISAR laser. The target sample is then glued into the target holding plate and made ready for the impact experimentation.

b.   Ceramet

Due to the high tolerance of the sample provided, no lapping was required to improve the flatness of the target. Although no lapping was required, there was still a need to roughen the surface measured by the VISAR due to the near mirror finish of the

33
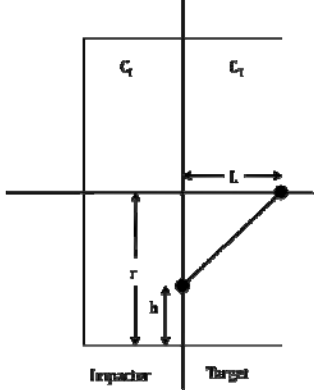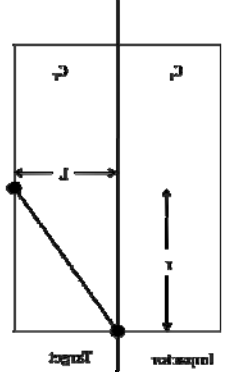
sample. This roughening was accomplished by lapping the VISAR side of the target sample with diamond paste. Typically 5 µm diamond paste was used for this roughening process.

7.   Design of Experiments

a.   *Edge Effects*

In order to ensure that fundamental assumptions of a uniaxial strain conditions holds true for the experiments conducted, estimation must be made for releases from the edge of a shock-compressed sample. This estimation will help to verify if the inwards radial propagation of release waves generated at the outer edge of the sample 'pollute' the region of 1-D strain. Due to the fact that information about the sound speed in the compressed state as a function of stress is usually not known for the target material, this it can only be an estimate. Table 2 shows the equations used for the estimation of the time of arrival of the edge release to the center of the sample where C_I and C_T are the sound speeds of the impactor and target, respectively.

Table 2.　　Equation used for estimating edge release.

$$t = \frac{r}{C_1} + \frac{l}{C_1}\sqrt{\frac{C_1^2}{C_T^2} - 1}$$ where $C_1 > C_T$	
$$t = \sqrt{\frac{r^2 + l^2}{C_T}}$$ where $C_1 \leq C_T$	

b.　　*Spall Location*

For symmetrical impact, spall measurement experiments are usually conducted with impactor having half the thickness of the target sample to result in the spall occurring in the middle of the target. In a situation where asymmetrical impact is done, or the thickness of the sample cannot be changed, checks have to be made to ensure that spall occurs somewhere in the middle of the target so that proper measurement of spall strength can still be made. This estimation can be made using simple x-t diagrams as shown in Figure 24.

35
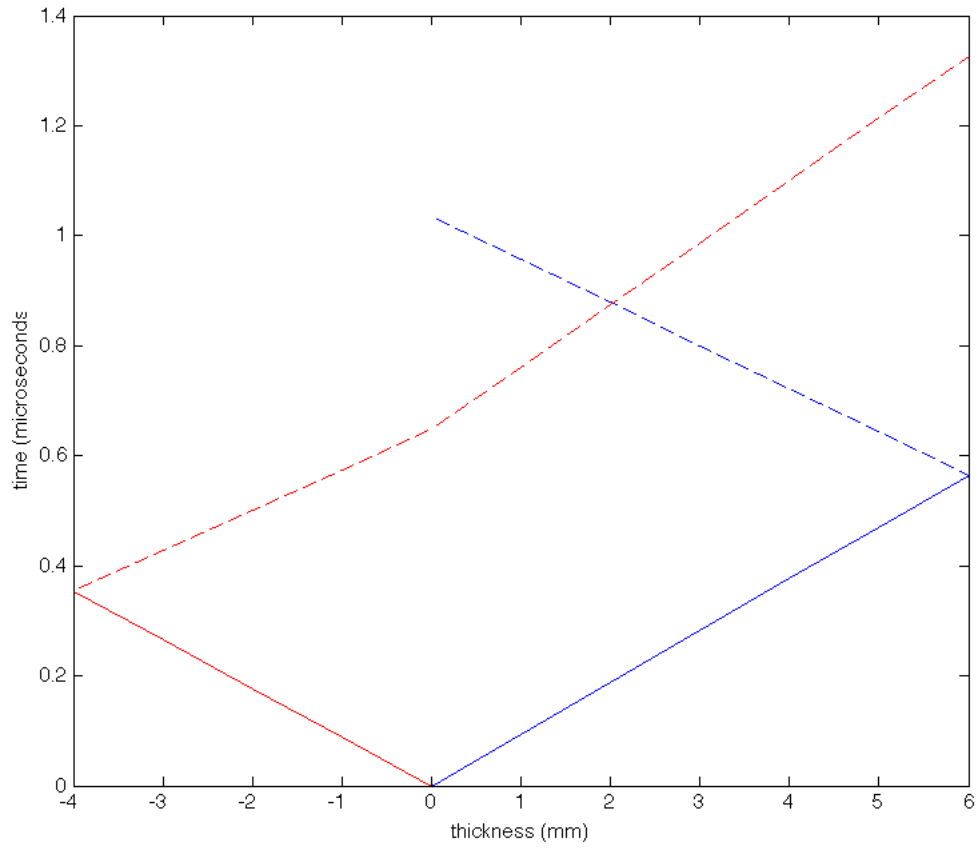
Figure 24.   x-t diagram illustrating interaction of release wave in unsymmetrical impact
experiment

In order to simplify the process of checking this for every experiment
conducted, a Matlab code was formulated (see Appendix A).

IV. EXPERIMENTAL RESULTS

In this section, results of all the experiments conducted for the purpose of this thesis will be presented. Data obtained along with the relevant analyses will be presented here.

A. CERAMIC CORBIT-98 SHOTS

As mentioned in Denzel (2010), Shot 10_3, which was the only shot performed in NPS for the purpose of measuring spall strength of Corbit-98 was not successful. This is suspected to be due to "micro-jetting" of the sample surface that destroyed the reflectivity of the foil and thus prevented any spall signature from being recorded. One of the objectives of this thesis was the continuation of the research on Corbit-98 and this section documents the shots performed to determine the spall strength.

1. Shot 10_13: Ceramic Corbit-98 Spall Shot

The first planar impact experiment conducted for the purpose of this thesis was designed to measure the spall strength of Corbit-98 in a way that was similar to shot 10_3. A thin layer of steel foil (12.7 μm thick) was glued to the back (VISAR side) of the ceramic sample for the purpose of reflecting the VISAR laser. Planned velocity was 0.25 km/s and based on the gas breech performance curve. The necessary pressure to achieve this velocity was approximately 590 psi. The actual velocity measurement yielded 0.2548 ± 0.0028 km/s with an indicated tilt of 2.04 mrad.

The ceramic Target Sample was measured to be 6.179 mm thick in the center with approximately a tilt of 30 μm between surfaces of the target holding plate and the sample itself. A single crystal (z-cut) sapphire was used as an impactor. The impactor was backed with a piece of 4.96 mm thick closed cell foam. The inclusion of the foam was necessary to provide a very low shock impedance boundary at the back of the impactor so that a deep release wave can be created for the purpose of spalling the sample.
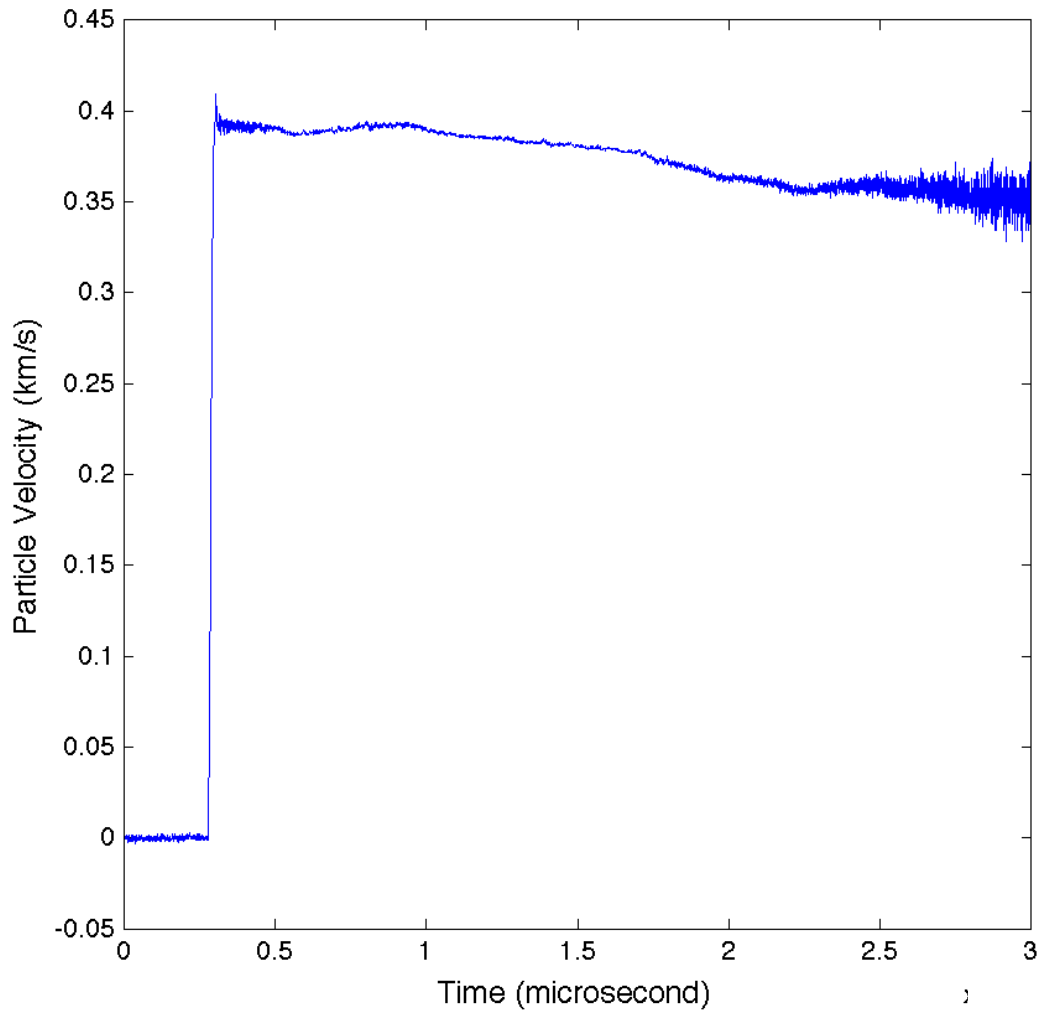
Figure 25.   Wave profile of ceramic Corbit-98 spall shot10_13

From Figure 25, no clear spall signature could be observed and it is speculated to be again due to the foil ejecting off the ceramic target sample as mentioned by Denzel (2010). Based on theoretical calculation, the approximate particle velocity was expected to be 0.131 km/s but this was not observed from the wave profile generated by the VISAR system.   Nonetheless, shock transit time through the sample could still be determined and a theoretical particle velocity could still be derived from the projectile velocity measured by the velocity pins.

2.   Shot 10_21: Ceramic Corbit-98 Spall Shot

Due to the possibility of the steel foil being ejected off the back of the target sample in the previous ceramic spall shot, another spall shot was setup without the use of the foil. In order to ensure that sufficient light was reflected from the back of the target sample to provide VISAR signal, the sample target was further lapped with a 6 μm diamond suspension solution on a Buehler mechanically driven polisher. Even after being polished, the VISAR laser had to be set to twice the usual wattage before reasonable signal amplitude could be obtained.

The planned projectile velocity was 0.2 km/s and the required breech pressure to drive the projectile is calculated to be 388 psi based on the weight of the projectile. The ceramic sample was measured to be 6.169 mm thick in the center with an approximate tilt of 30 μm between surfaces of the target holding plate and the sample itself. A single crystal (z-cut) sapphire was used as the impactor. An air pocket was created at the back of the impactor instead of the foam used in the previous shot for the purpose of creating a very low shock impedance boundary.
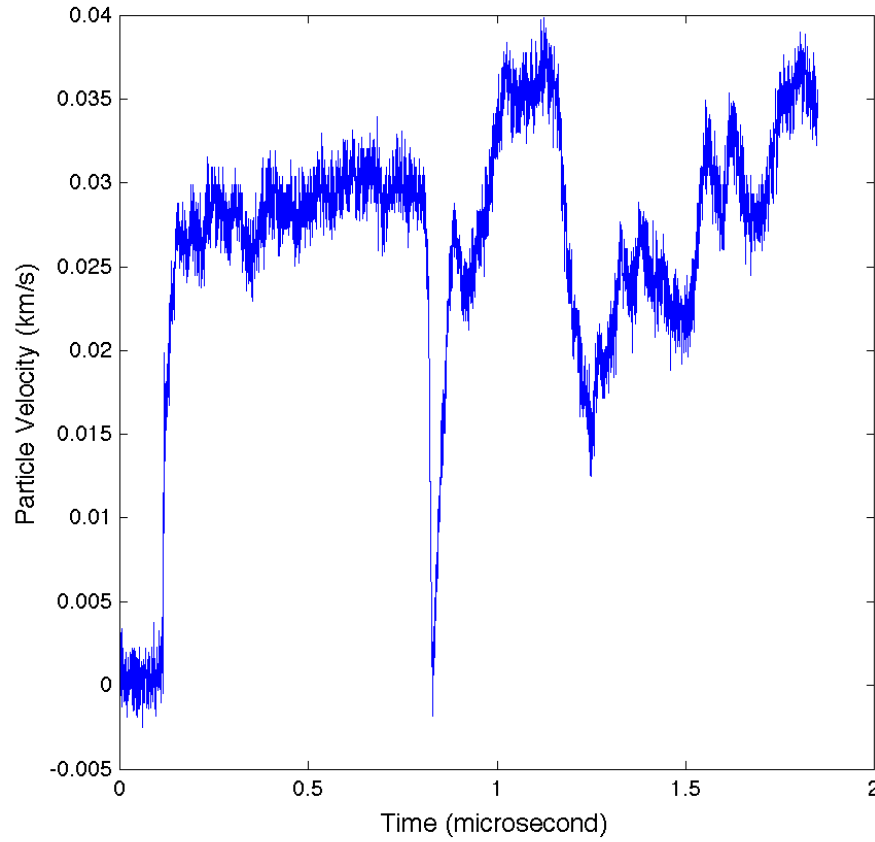
Figure 26.   Wave profile of ceramic Corbit-98 spall shot10_21

From Figure 26, no clear spall signature could be observed and peak particle velocity observed was a low of 0.03 to 0.04 km/s. As this is a symmetrical impact experiment, the expected U_{fs} should be 0.2 km/s. This unusually low particle velocity and the lack of spall signature indicated that the experiment has failed. The possible reason of this unsuccessful shot could be due to micro jetting, due to the shockwave created by the planar impact hitting the imperfect ceramic surface caused micro jets to form and thus resulted in unusual data recorded by the VISAR system.

The flyer speed measured by the velocity pins was 0.204 $\pm$ 0.004 km/s with a tilt of 4.067 $\pm$ 2.256 mrad. Due to the slow flyer speed, the timing setup for the oscilloscope was too short, and so the time of impact could not be recorded. 'Both9.txt' (see Appendix B) was the file used for this experiment and was later modified to 'Both11.txt'

40

(see Appendix C) in order to be able to record the impact time for the subsequent experiment conducted at this low flyer speed. Without the time of impact, shock speed and particle velocity cannot be determined for this experiment.

3.   Shot 10_23: Ceramic Corbit-98 Spall Shot

With the unsuccessful trial of experimenting without the use of foil, Shot 10_23 was setup again using a foil at the VISAR side of the target sample. The foil used was 0.3 μm made of stainless steel. In order to ensure enough light was reflected back to the VISAR probe, the foil was roughened up with a 10 μm diamond paste.

The planned velocity was 0.2 km/s and the required breech pressure to drive the projectile is calculated to be 389 psi based on the weight of the projectile measured. The ceramic sample was measured to be 6.165 mm thick in the center with an approximate tilt of 30 μm between surfaces of the target holding plate and the sample itself. A single crystal (z-cut) sapphire was used as the impactor. An air pocket was created at the back of the impactor instead of the foam used in the previous shot for the purpose of creating a very low shock impedance boundary.

The impact time of the projectile was successfully measured using the flush pins. The flyer speed measured by the velocity pins was 0.2104 ± 0.001 km/s with a tilt of 1.745 ± 0.6854 mrad. On this last and final experiment conducted to investigate the spall strength of Corbit-98, the VISAR generated wave profile again failed to record any spall signature as shown in Figure 27.
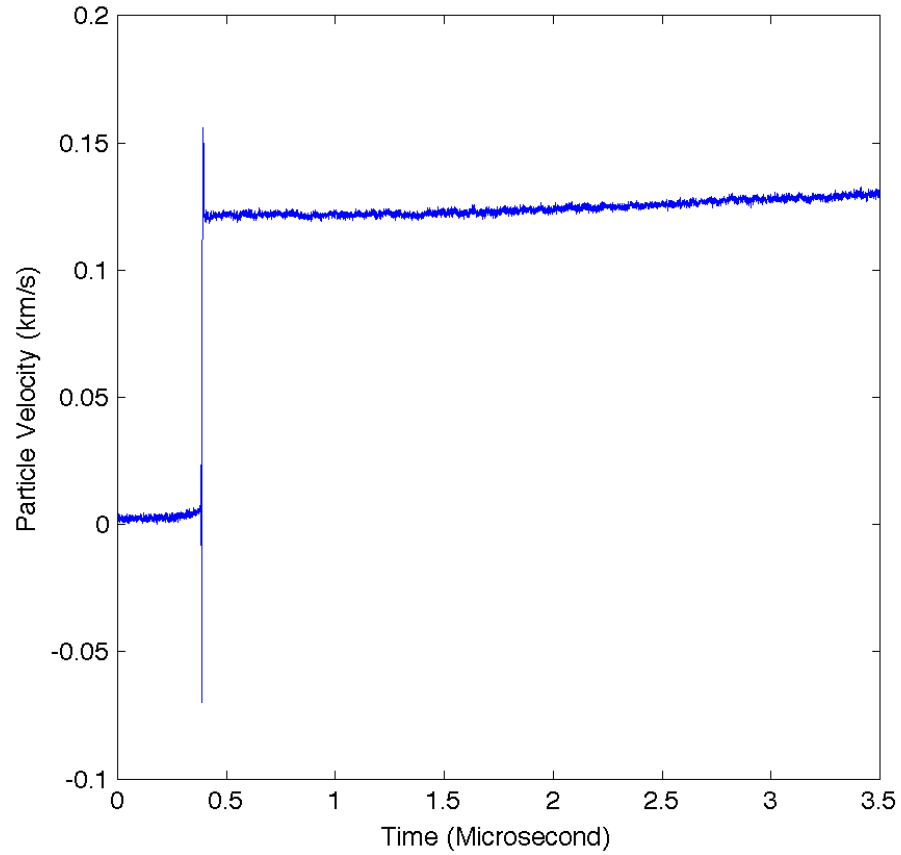
Figure 27.   Wave profile of ceramic Corbit-98 spall shot10_23

B.   CERAMET TUNGSTEN CARBIDE SHOTS

An investigation into a new super hard material is also an objective of this research. The new material in focus for this section of the thesis is a metal-ceramic composite material generally referred to as ceramet (Tungsten Carbide in a Cobalt matrix). Here we tested two different kinds of this material, called GC-330 and GC-915. Three shots were performed on the more dens GC-915 material and of the 3 shots, 2 were designed to be a free surface shot and 1 was designed to be a window shot. As for GC-330, only 1 free surface shot was performed. Appendix D includes the specifications sheets for these materials.

1.   Shot 10_14: Ceramet Tungsten Carbide Spall Shot

The first Ceramet shot conducted was designed to be a free surface shot for the purpose of determining the spall strength as well as obtaining information on the shock Hugoniot of this material. This shot was setup as a symmetrical planar impact with the impactor having a thickness of 4.00 mm and the target having a 7.996 mm thickness. The diameters were identical, measuring: 50 mm. With symmetrical impact as well as the selected thickness of impactor and target sample, the spall is predicted to occur close to the middle of the target sample.

Diagnostics used for these experiments include velocity pins, PZT pins and the VISAR systems. Due to the mirror like reflectivity of the Ceramet target sample, there was a need to roughen the surface for a more diffuse reflection of the laser beam from the VISAR. This is necessary to ensure that the VISAR probe can receive the reflected laser for the purpose of recording the free surface motion of the target sample. The roughening of the surface was done with the use of 5um diamond paste as shown in Figure 28.

Figure 28.   Diamond paste used for roughening of sample surface

Both surfaces of the target and impactor were measured to have a tilt of <5 μm between surfaces. Just as for the ceramic spall shot, an air pocket was created right

behind the impactor for the purpose of providing a very low shock impedance boundary at the back of the impactor so that a deep release wave is reflected. The mass of the projectile with the impactor and with the O-rings mounted was 552.9 g. Using the gas breech performance curve, the calculated pressure to achieve a desired projectile velocity of 0.2 km/s was 446 psi.

From the data recorded by the velocity pins, the tilt was derived to be 1.95 ± 0.182 mrad and a projectile velocity of 0.209 ± 0.0002 km/s. Shock transit time based on the impact time of the flush PZT pins and the first arrival of shock recorded by the VISAR system was 1.091 μs. Due to offsets between the target and the flush PZT pins, the height differences must be taken into account and the corrected shock transit time was 1.212 μm. The shock speed was calculated to be 6.599 km/s. As this is a symmetrical impact, the particle velocity U_P can be taken to be $0.5 * U_D$ (Projectile Velocity) or 0.105km/s.

Figure 29.   Shot 10_14 wave profile featuring spall signature

44

Finally, the approximate spall strength was calculated to be 2.11 GPa using the pull back spall signature shown in Figure 29. As mentioned earlier in the Chapter III, we cannot precisely determine the spall strength from use of bulk sound speed as the wave speed in this calculation for brittle materials. However, for simplification, we knowingly use it to acquire an approximate value of spall strength.

2. Shot 10_18: Ceramet Tungsten Carbide Spall Shot

A second spall experiment was also performed to verify the results of the previous spall shot and at the same time, obtain another data point on the shock Hugoniot. Experimental setup was exactly as per described above for the previous ceramet spall shot 10_14 with the exception of a higher projectile velocity. The mass of the projectile with the impactor and with the O-rings mounted was 552.9 g. From the gas breech performance curve, the calculated pressure to achieve the desired projectile velocity of 0.3 km/s was 1010 psi.

Wave profile generated by the VISAR system was of very high quality. The spall signature could be clearly observed as shown in Figure 30.
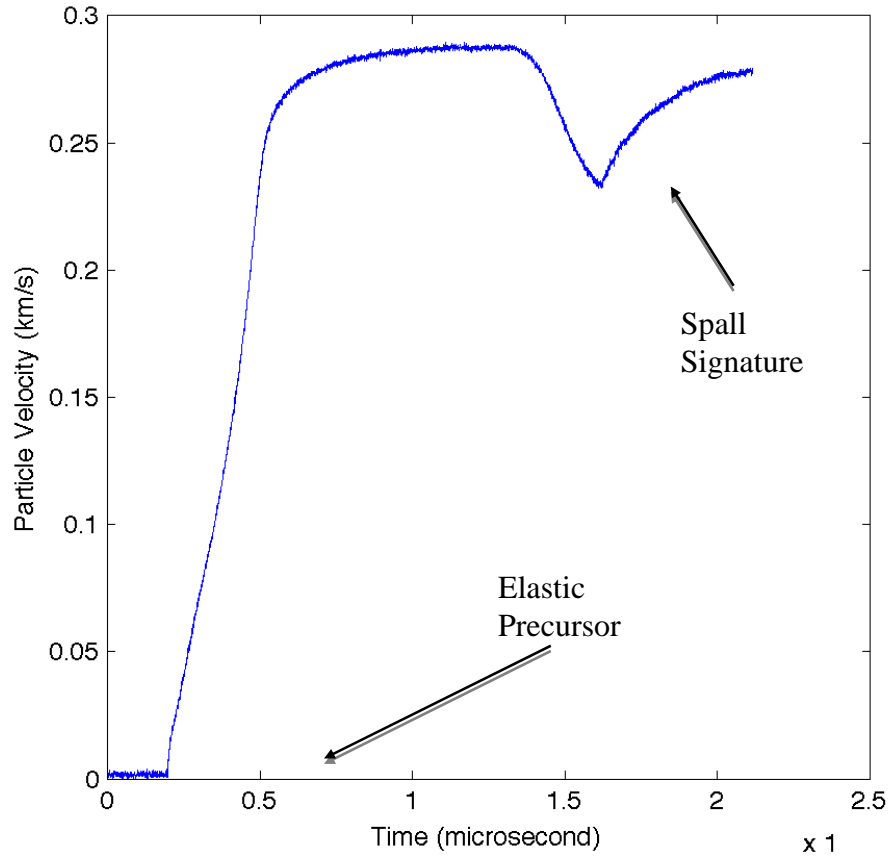
Figure 30.   Shot 10_18 wave profile featuring spall signature

From the data recorded by the velocity pins, the tilt was derived to be 1.326 $\pm$ 0.37 mrad and a projectile velocity of 0.300 $\pm$ 0.001 km/s. Shock transit time based on the impact time from flush PZT pins and the first arrival of shock recorded by the VISAR system was 1.1565 μs. Due to imperfections from mounting the target and PZT pins, height differences must be taken into account and the corrected shock transit time was 1.2039 μs. From the target thickness and the transit time, the shock was calculated to be travelling at 6.639 km/s. As this is a symmetrical impact, the particle velocity U_P can be taken to be $0.5 * U_D$ (Projectile Velocity) or 0.1504 km/s. Fi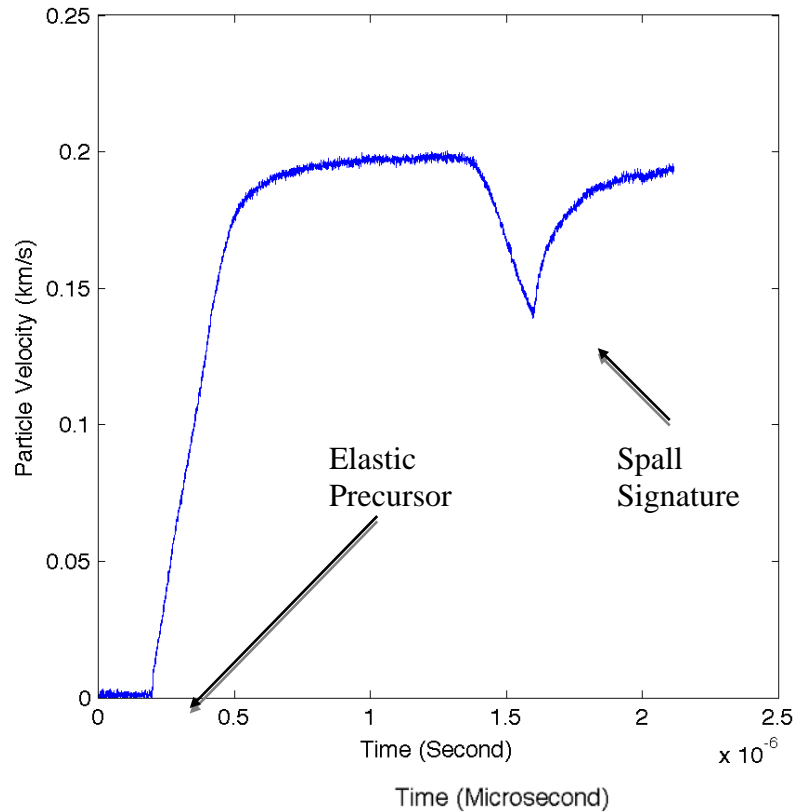nally, the approximate spall strength was calculated to be 1.959 GPa using the equation $\sigma_{spall} = \frac{1}{2}\rho_o C_B \Delta U_P$.   As mentioned earlier in the Chapter III, we cannot precisely determine the spall strength

from use of bulk sound speed as the wave speed in this calculation for brittle materials. However, for simplification, we knowingly use it to acquire an approximate value of spall strength.

3. Shot 10_19: Ceramet Tungsten Carbide Window Shot

As opposed to the previous two shots conducted for the ceramet, Shot 10_18 was designed to be a window shot. With the use of a window, an almost in-situ measurement of the particle velocity history could be obtained. A sapphire window was used in this experiment and as before, the surface observed by the VISAR system was roughened using 6μm diamond paste before gluing the sapphire window onto the back of the target sample.

In order to measure the HEL of this ceramet, a higher projectile velocity is desired to increase the impact pressure. The experiment was setup to throw the projectile at 0.35 km/s. In order to reach this velocity without using exceedingly high breech pressure, the generic projectile normally used was bored out internally to lower the mass to 447.6 g. The required breech pressure was estimated to be 1,100 psi with the use of the gas gun performance curve to achieve this required projectile velocity.

This shot was setup as a symmetrical planar impact with the impactor measured at 4.00 mm thickness at the center and the target measuring 7.993 mm thickness at the center—the diameters were the same as before. With symmetrical impact, the U_P can be taken to be $0.5 * U_D$ (Projectile Velocity). Both surfaces of the target and impactor were measure to have a tilt of <5 μm between surfaces.
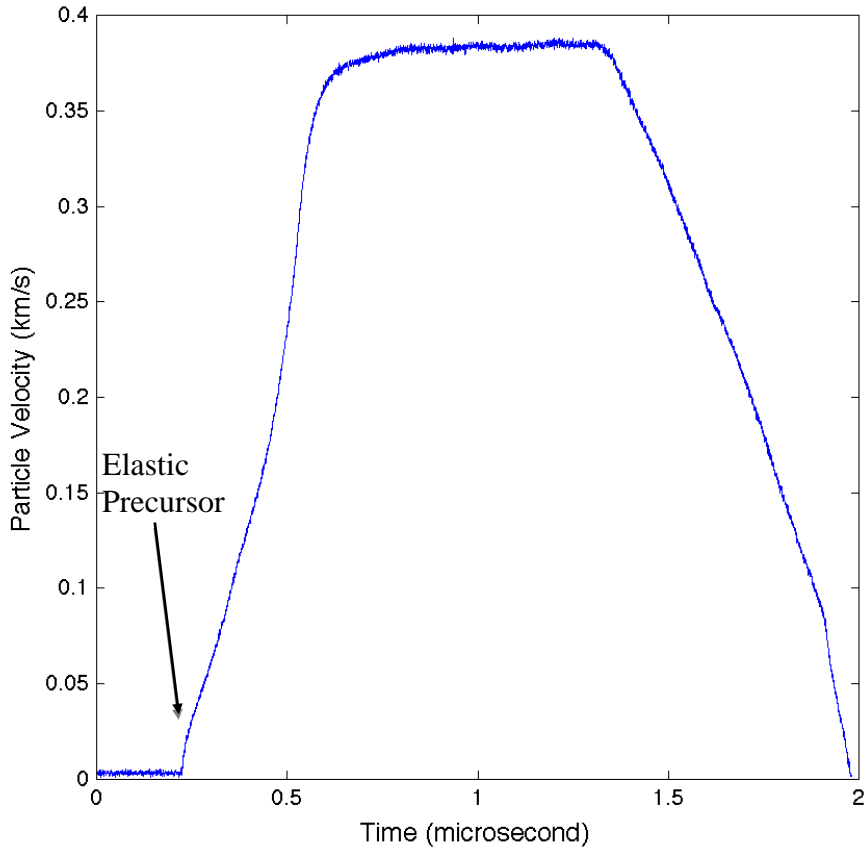
Figure 31.   Shot 10_19 wave profile of a window shot

All diagnostics used correctly recorded excellent data. As shown in Figure 31, the wave profile generated by the VISAR system was of very high quality and a subtle precursor was observed at the toe of the wave profile. Based upon the shorting time of the velocity pins, the projectile was calculated to be travelling at 0.35 ± 0.001 km/s and had a tilt of 2.987 ± 0.604 mrad. Taking into account the imperfections in mounting of the target sample and the PZT flush pins, the shock transit time was corrected to 1.080 µs and the resulting shock speed U_S was calculated to be 7.402 km/s. The particle velocity U_P was taken to be $0.5 * U_D$ (Projectile Velocity) or 0.175 km/s.

4. Shot 10_20: GC-330 Ceramet Tungsten Carbide Spall Shot

This final experiment conducted on a ceramet was done to compare the shock Hugoniot of a less dense ceramet (GC-330). The experiment was designed to be a free surface, symmetrical planar impact. The experimental setup was close to shot 10_18 with the exception of a lower breech pressure (990 psi) used for this experiment. Although the projectile is fired at the same velocity of 0.3 km/s, a lower pressure was required due to a less dense impactor, which brings down the mass of the projectile.
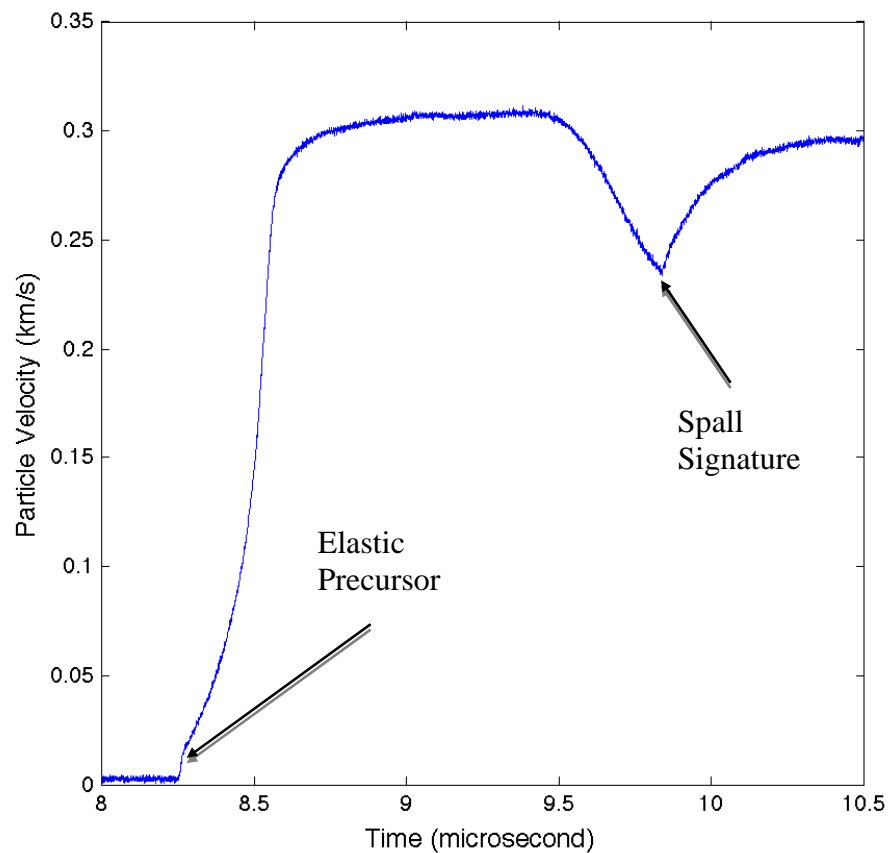
Figure 32.   Shot 10_20 wave profile of a window shot

As shown in Figure 32, the wave profile generated by the VISAR system is of very high quality and spall signature can be clearly observed. From the velocity pins, the projectile was calculated to have a velocity of 0.318 $\pm$ 0.001 km/s and a tilt of 1.241

± 0.366 mrad. Shock transit time was measured to be 1.218 µs but corrected to 1.287 µs after taking into account the imperfection of the mounting of the target and PZT pins. The shock speed U_S was calculated to be 6.216 km/s based on the transit time and thickness of the target. The particle velocity U_P can be taken to be $0.5 * U_D$ (Projectile Velocity) or 0.159 km/s due to symmetrical impact. Finally, the approximate spall strength was calculated to be 2.284 GPa.

V. DISCUSSION OF RESULTS

A. UNCERTAINTY ANALYSIS

In order to understand how accurate the measurements described above are, there's a need to look at the potential sources of uncertainty and make an estimate using standard techniques. In this section, the principal sources of error are measured in *distances* and *times*.

Due to the design of the gas gun (throwing projectile at very low speed), a much higher shock speed exists in the target sample as compared to the projectile velocity, and this results a relatively short shock transit time. This results in a large uncertainty when it comes to establishing shock transit time, because small distance offsets in flush pins lead to relatively large time offsets. With the assumption of a Gaussian distribution of uncertainty, fractional uncertainty in shock velocity can be calculated based on the equation below:

$$\frac{\Delta U_s}{U_s} = \sqrt{\left(\frac{\Delta x}{x}\right)^2 + \left(\frac{\Delta t}{t}\right)^2} \tag{20}$$

Although the electronic measuring equipment in the lab allows for measurement of up to $1 - 2$ μm, the limiting factor lies in the flatness of the sample target and how parallel the front and back surfaces are to each other. Therefore, Δx is based on the flatness tolerance measured where x is the thickness of the sample. Δt was set at 15 ns which is the resolution of time the diagnostics can measure to and t is the transit time measured. Table 3 summarizes the values used for the calculations of uncertainty in measured shock velocity.

Table 3.   Values used for calculating uncertainty

	Ceramic			Ceramet			
	Shot10_13	Shot10_21	Shot10_23	Shot10_14	Shot10_18	Shot10_19	Shot10_20
Δx (mm)	0.010	0.015	0.0013	0.003	0.003	0.003	0.003
x (mm)	6.179	6.169	6.165	7.996	7.993	7.993	8.003
$\dfrac{\Delta x}{x}$ (%)	0.16	0.24	0.02	0.04	0.04	0.04	0.04
Δt (ns)	15	15	15	15	15	15	15
t (μs)	0.571	-	0.573	1.211	1.204	1.08	1.287
$\dfrac{\Delta t}{t}$ %	2.63	-	2.62	1.24	1.25	1.39	1.17
$\dfrac{\Delta t}{t}$	2.63	-	2.62	1.24	1.25	1.39	1.17

Another potential source of uncertainty lies in the correct calculation of shock stress. With the assumption of very good measurement of initial density of sample target used, uncertainty of shock stress can be easily calculated with Equation 21:

$$\frac{\Delta P}{P} = \sqrt{\left(\frac{\Delta U_s}{U_s}\right)^2 + \left(\frac{\Delta U_D}{U_D}\right)^2} \tag{21}$$

The uncertainty of in impact velocity was determined through the use of a least square fit on the shorting time of the velocity pins. Using the uncertainty of the shock speed derived in earlier, the calculated uncertainties for the respective shock stresses are tabulated in Table 4.

Table 4.   Values used for calculating shock stress uncertainty

	Ceramic			Ceramet			
	Shot10_13	Shot10_21	Shot10_23	Shot10_14	Shot10_18	Shot10_19	Shot10_20
$\dfrac{\Delta U_S}{U_S}$ (%)	2.63	-	2.62	1.24	1.25	1.39	1.17
$\dfrac{\Delta U_D}{U_D}$ (%)	1.10	1.96	0.48	0.96	0.33	0.35	0.31
$\dfrac{\Delta P}{P}$ (%)	2.63	-	2.62	1.24	1.25	1.39	1.17

B.   CEARMIC CORBIT-98

1.   Spall Strength

As a continuation of previous NPS research performed by Denzel (2010), the main focus on ceramic Corbit-98 was to establish and verify the spall strength as well as adding more data points on the shock Hugoniot in the U_S vs U_P plane. Unfortunately, all free surface planar impact experiment conducted on the NPS gas gun untill the present date has failed to record any clear spall signature. Mentioned earlier in Chapter IV, jetting from the porous surface of the ceramic sample is the most likely cause of this.

2.   Hugoniot

Table 5.   Hugoniot data of Corbit-98

Shot	Material	Type	U_D (km/s)	U_S (km/s)	U_P (km/s)	P (GPa)
10_13	Corbit 98	FS	0.254	10.81	0.1325	5.515
10_21	Corbit 98	FS	0.204	-	-	-
10_23	Corbit 98	FS	0.210	10.756	0.1328	5.499

Values for the elastic Hugoniot for the ceramic shots conducted for the purpose of this thesis are summarized in Table 5. Due to the free surface micro-jetting effects described above, U_P as measured from the wave profile cannot be accurately used for the calculation of the pressure state attained. Therefore, U_p was calculated based on impedance matching method using the measured U_D and U_S. In order to simply the process, a simple Matlab® code (see Appendix E) was generated for the purpose of this calculation.

$$U_S = 0.959 * U_P + 10.57$$
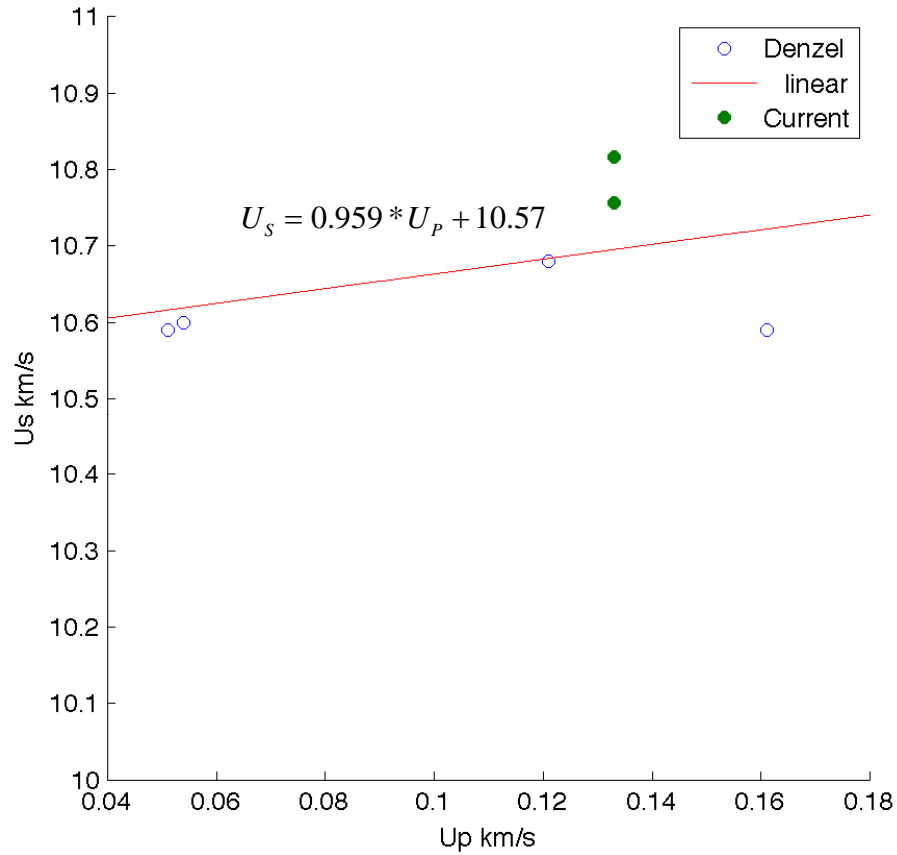
Figure 33.   Compiled Hugoniot data for ceramic (After Denzel, 2010)

The elastic Hugoniot for Ceramic is particularly difficult to measure due to the fact that a slow projectile velocity with high shock velocity in target sample can result in large time uncertainties with just a small distance uncertainties. From Figure 33, it can be observed that the current data are in reasonable agreement with the Hugoniot

54

previously measured by Denzel (2010), changing only slightly from the previous $U_S = 10.53 + 0.936U_p$ to the current derived Hugoniot of $U_S = 10.57 + 0.9591U_p$. With the inclusion of the two more data points from the experiment of this thesis, the new elastic Hugoniot found is a good starting point for computer simulation of Corbit-98.

C.   CERAMET TUNGSTEN CARBIDE

1.   Hugoniot

Table 6.   Hugoniot data obtained for Ceramet Tungsten Carbide

Shot	Material	Type	U_D (km/s)	U_S (km/s)	U_P (km/s)	P (GPa)
10_14	GC-915	FS	0.209	6.599	0.105	9.276
10_18	GC-915	FS	0.301	6.639	0.150	14.006
10_19	GC-915	SW	0.350	7.402	0.175	18.154
10_20	GC-330	FS	0.318	6.216	0.159	12.351

Table 6 shown above summarizes all the Hugoniot data collected for the Ceramet Tungsten Carbide experimented in support of this thesis. Figures tabulated are already corrected for the imperfections of the mounting of the sample and PZT pins. Using the data in Table 3, the U_S-U_P plot is as shown in Figure 34 and the linear fit is based solely on GC-915 data only. The GC-330 data point is shown for completeness only.

$$U_S = 10.2 * U_P + 5.42$$
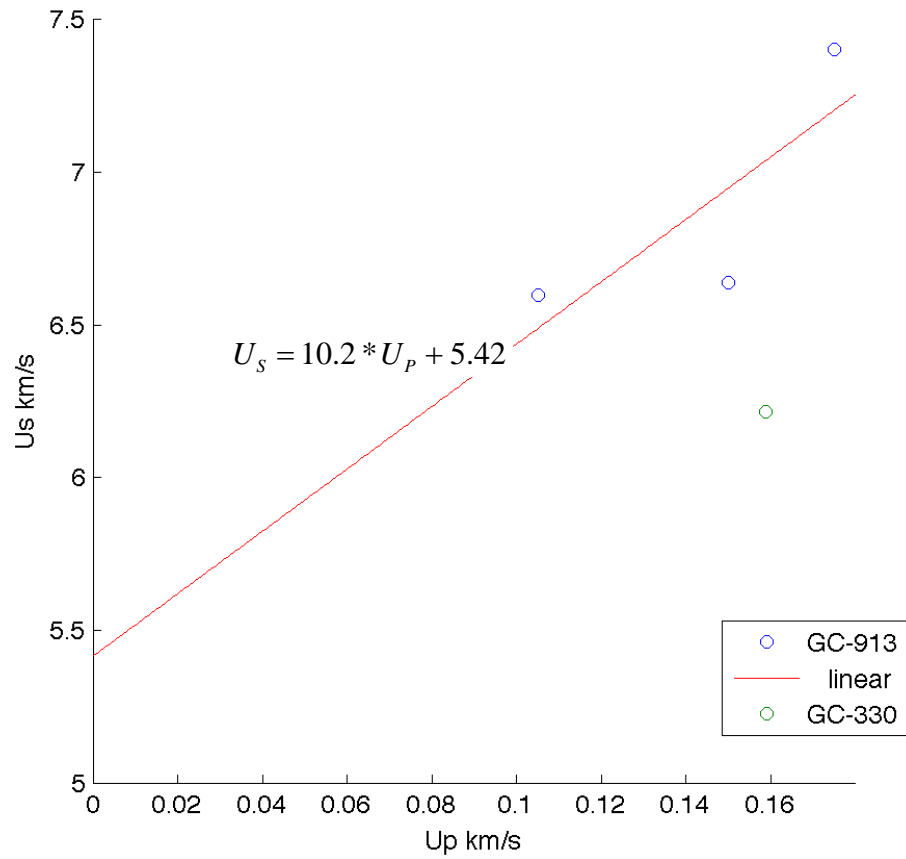
Figure 34.   Hugoniot plot of NPS ceramet data

2.   Dynamic Strength

One of the main objectives of this research was to determine the compressive dynamic yield strength for Ceramet Tungsten Carbide. In order to do this, there is a need to shock the sample to a pressure state above the yield point. Due to velocity limitations of the single stage gas gun used for the purpose of this research, the maximum stress state achievable is not significantly higher than the HEL. Figure 35 shows the plot of the compression shock profile of the ceramet experiment conducted for this research:
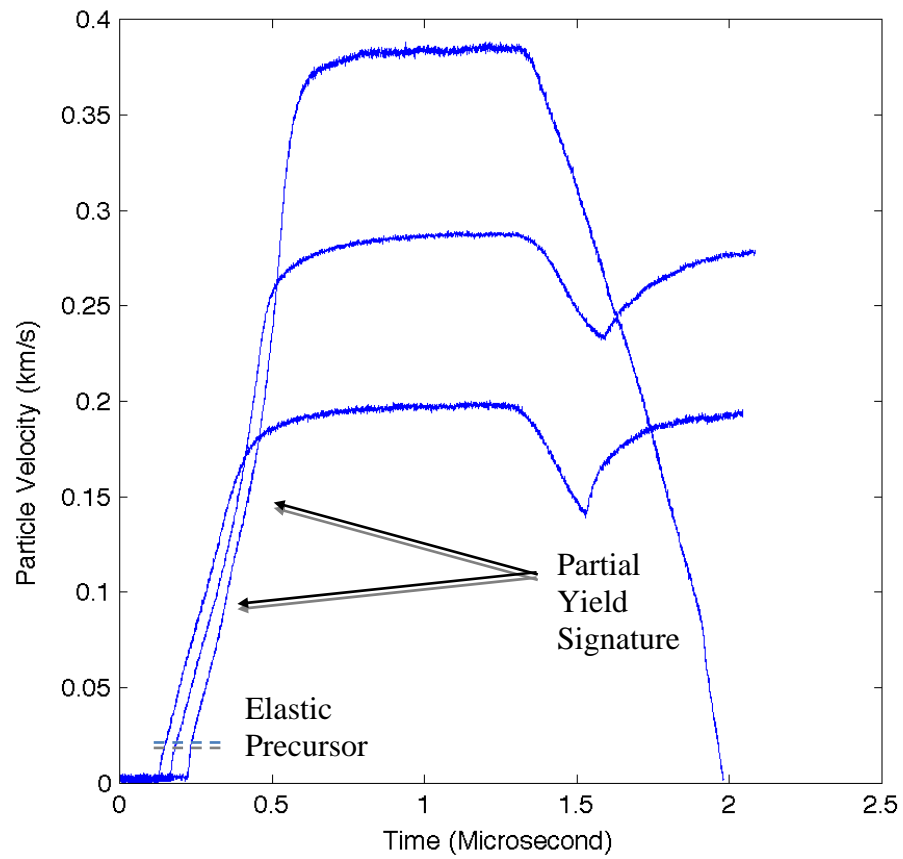
Figure 35.   Compression shock profiles for tungsten carbide

From Figure 35, it can be observed that the compression shock profile of NPS does not display a distinct transition from the elastic precursor rise to the transition ramp region. This phenomenon was also observed by Grady (1995).
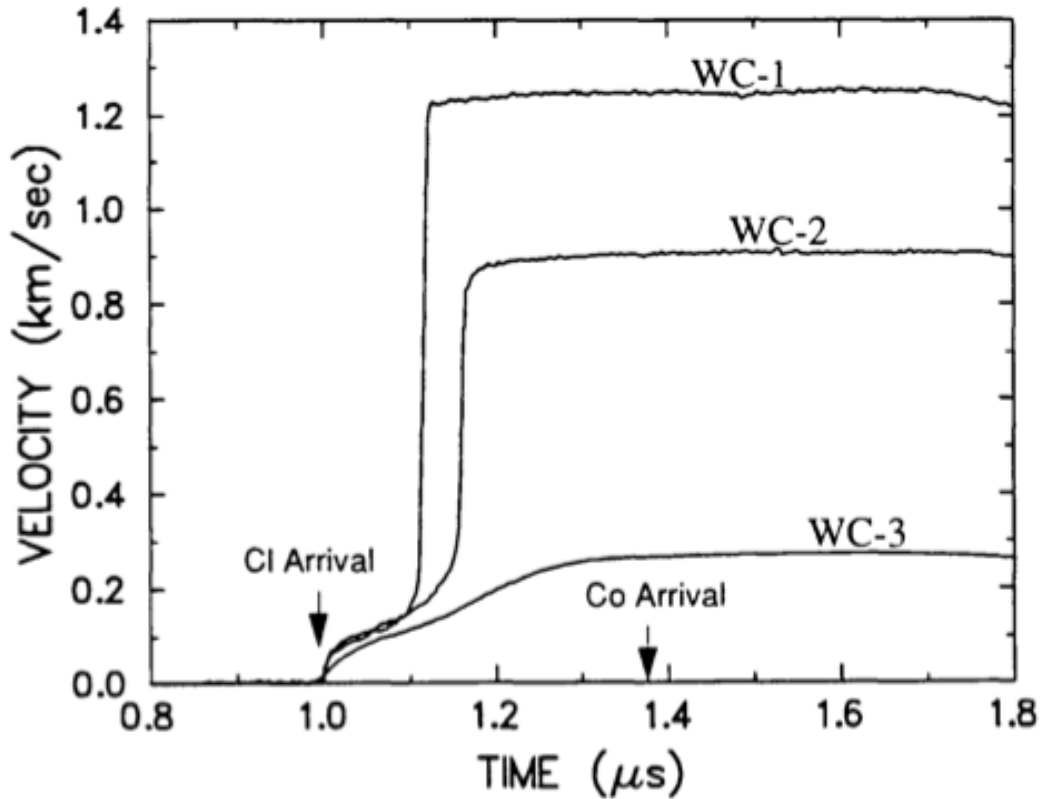
Figure 36.   Compression shock profiles for tungsten carbide (From Grady, 1995)

From Figure 36, it can be observed that WC-3 compression shock profile did not provide a distinct transition level as WC-1 and WC-2. It is noteworthy that both WC-3 and NPS compression shock profiles are at a low peak U_P of 0.2 to 0.3 km/s. By firing at higher impact speeds, larger shock amplitudes will be reached that should provide a more distinct yielding transition as those observed in Grady's WC-2 and WC-1 profiles in Figure 35.

There is a consistent transition point at approximately 0.01 km/s that indicates the start of the yielding process (i.e., HEL stress). Based on a shock impedance calculation this leads to a HEL of 0.935 GPa. However, we believe this is just the beginning point for a complex yielding process that is spread out over a broad range of particle velocity and stress. In our wave profiles, we see one and perhaps two changes in slope (slightly above Up of 0.1 km/s and a more distinct change slightly below 0.15 km/s). These may suggest

that the HEL point at 0.01 km/s indicates the onset of a partial yielding process and the 0.15 km/s point shows a full yielding process. The intricacies of this complex yielding are far beyond the scope of this thesis and more data will be needed to obtain a better understanding of this process. We have been collaborating with Prof. Zok at UCSB and one of his PhD students, Mr. Brett Compton, will be investigating this complex yielding phenomena.

3. Spall Strength
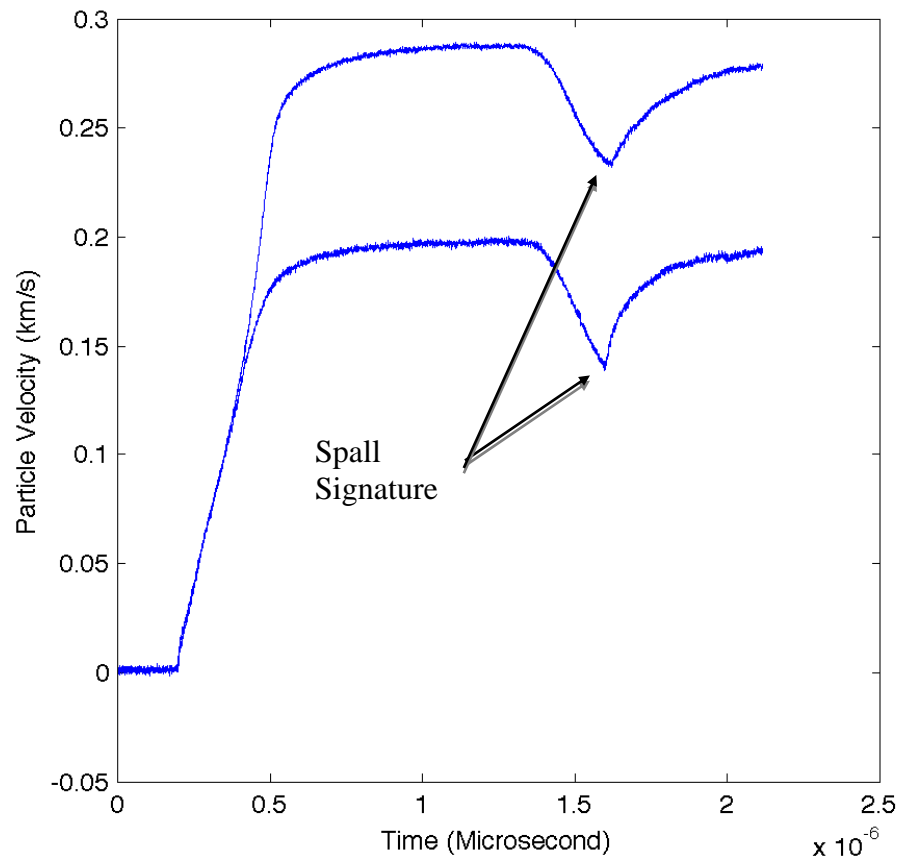
Figure 37. Wave profiles of NPS tungsten carbide spall shots

59

Clear spall signatures can be easily observed for all the wave profiles obtained as shown in Figure 37. These clear signatures indicated that the material has completely spalled. The spall strength of tungsten carbide can then be calculated from the spall pullback signal identified in the compression shock profile.

Similar to ceramic materials, it is not rigorous to use bulk sound speed to calculate the spall strength as would be done for metal that is of a more ductile nature. Therefore the spall strength calculated here is only an approximation done for comparison, and a small error will exist in our calculated values. A more rigorous analysis of these data is also beyond the scope of this thesis.

Table 7.   Spall properties of tungsten carbide

Shot	Material	U_{max} (km/s)	U_{min} (km/s)	σ_{spall} (GPa)
10-14	GC-915	0.2003	0.139	2.11
10-18	GC-915	0.289	0.232	1.96
10-20	GC-330	0.31	0.234	2.28

Table 7 summaries spall strength calculated from the present data. The bulk sound speeds used in the above calculation are 4.69 km/s and 4.9 km/s for GC-915 and GC-330 respectively. A reasonable agreement with the spall strength of between 2.62–3.56 GPa as reported by Grady (1995).

VI. CONCLUSIONS

From the experiments performed herein, fundamental dynamic loading properties for both ceramet tungsten carbide GC-915 and GC-330 were found. A summary of the results are tabulated in Table 8.

Table 8.   Summary of results

Shot	Material	Type	U_D (km/s)	U_S (km/s)	U_P (km/s)	σ_{spall} (GPa)	P (GPa)
10_13	Corbit 98	FS	0.254	10.81	0.1325	-	5.515
10_21	Corbit 98	FS	0.204	-	-	-	-
10_23	Corbit 98	FS	0.210	10.756	0.1328	-	5.499
10_14	GC-915	FS	0.209	6.599	0.105	2.11	9.276
10_18	GC-915	FS	0.301	6.639	0.150	1.96	14.006
10_19	GC-915	SW	0.350	7.402	0.175	N.A.	18.154
19_20	GC-330	FS	0.318	6.216	0.159	2.28	12.351

With 3 planar impact experiments conducted for GC-915 tungsten carbide, there is enough information on the Hugoniot in U_S-U_P plane to best fit a Hugoniot relationship as follows:

$$U_S = 10.2 * U_P + 5.42$$

Since the Hugoniot relationship for tungsten carbide is only derived based on 3 points, there's still a fair amount of uncertainty and a few more experiments are recommended to verify the reliability. Above all, the experiments conducted for the purpose of this thesis were only performed at relatively low impact velocity due to the limitation of the NPS gas gun. Although these low impact velocities give us a good preview of the dynamic loading response of the material tested, it is necessary to conduct similar experiments at a higher stress state to obtain fast rising plastic waves and be able to better understand the yielding process.

With regards to the ceramic, we were able to obtain additional Hugoniot data that reinforces the EOS obtained by Denzel (2010). Our Hugoniot EOS changes only slightly

from the previous $U_S = 10.53 + 0.936U_p$ to the currently derived Hugoniot of $U_S = 10.57 + 0.9591U_p$. Due to micro jetting from the porous surface of the target sample, the generated VISAR wave profiles could not be used to determine the spall strength. More investigation into the experimental method for establishing spall strength is recommended for future research but is beyond the scope of this research.

Corbit-98 ceramic has low spall strength of 2.71 kbar (from only 1 experiment conducted by Denzel (2010)) illuminates the problem that alumina based ceramics have poor or no multi-hit capability for armor applications. Especially for the composite armor concept, the second wave spreading layer that is usually made of low impedance material, will reflect a release wave back into the ceramic layer causing it to spall. Although ceramet tungsten carbide has a spall strength of almost 10 times higher than Corbit-98 (2.11 GPa and 0.27 GPa, respectively), it is still relatively low, and the ideal first layer for the composite armor concept would be a material with high HEL and spall strength but such materials does not currently exist. Promising results have been shown in research of amorphous metals but these materials are also known to be relatively brittle. This inherent brittle response can be improved by having ductile dendritic inclusions gives amorphous metals the ability to limit the distances a crack can propagate and thus increasing the overall material's ductility. It is recommended that future work on planar impact experiments be conducted on amorphous/dendritic metals to better characterise their dynamic loading response. For now, small tiles of ceramic or even ceramet can be assembled to form the first layer in bid to obtain a better multi-hit capability for the composite armor concept.

With the new information acquired in thesis, simulation can now be improved for use in hydrodynamic codes. Using Johnson-Holmquist model with better input, a new computer simulation can be done based on Ongs (2009) work. Furthermore, new information on ceramet tungsten carbide is now available to be tested in the simulation model of the composite armor system. These simulations can then be used to compare with existing and new integral test results.

APPENDIX A: X-T DIAGRAMS MATLAB CODE

```matlab
%% Initial Condition
clc
clear all
rho2=3.85;      %Ceramic
rho1=3.985;      %Sapphire
c1=11.19;
c2=10.5;
s1=1;
s2=0.94;
Ud=0.25;
x1=-4:0;
x2=0:6;
%% Coefficient of quadratic equation
a=(rho1*s1-rho2*s2)
b=-(2*rho1*s1*Ud+rho1*c1+rho2*c2)
c=(rho1*s1*Ud^2+rho1*c1*Ud)
%% Solve quadratic equation
Upx1= -(b + (b^2 - 4*a*c)^(1/2))/(2*a)
Upx2= -(b - (b^2 - 4*a*c)^(1/2))/(2*a)
%% Ask for user's choice of Up2
Up2=input('Upx1 or Upx2 for Up2?    ')
%% Us2
Us2=10.5+0.94*Up2
%% First wave
t2=x2/Us2        %wave in ceramic
plot(x2,t2,'b')
hold all
Us1=-((Ud-Up2)+c1);
t1=x1/Us1        %wave in sapphire
plot(x1,t1,'r')
%% Reflected wave
t3=x2/(1.2*Us2)              %reflected wave in ceramic
plot (x2,fliplr(t3)+max(t2),'--b')
t4=x1/(1.2*Us1)
plot (x1,fliplr(t4)+max(t1),'--r')
plot (x2,t2*1.2+max(fliplr(t4)+max(t1)),'--r')
Timeofspall=max(t1)+4/(1.2*Us2)
```

THIS PAGE INTENTIONALLY LEFT BLANK

APPENDIX B: BOTH9.TXT

```
RunDig setup file.
Experiment description line

DEVICE:DPO4104:B020141
Digitizer use = VISAR
Factory
Select:CH1 ON;
CH1:Coupling DC;Impedance 50;Pos +4.0;Scale 0.02;
Select:CH2 ON;
CH2:Coupling DC;Impedance 50;Pos +4.0;Scale 0.02;
Select:CH3 ON;
CH3:Coupling DC;Impedance 50;Pos +4.0;Scale 0.02;
Select:CH4 ON;
CH4:Coupling DC;Impedance meg;Pos +4.0;Scale 0.02;
Horiz:RecordLength 100000;Scale 2E-6;delay:time 8.0e-6;
Trigger:A:Type Edge;
Trigger:A:Edge:Source EXT;Coup DC;Slope rise;
Trigger:A:Mode Normal;Level 1.00;

DEVICE:DPO4104:B020142
Digitizer use = pins
Factory
Select:CH1 ON;
CH1:Coupling DC;Impedance meg;Pos +3.0;Scale 1.00;
Select:CH2 ON;
CH2:Coupling DC;Impedance meg;Pos -4.0;Scale 10.0;
Select:CH3 ON;
CH3:Coupling DC;Impedance meg;Pos -4.0;Scale 10.0;
Select:CH4 ON;
CH4:Coupling DC;Impedance meg;Pos +0.0;Scale 0.05;
Horiz:RecordLength 100000;Scale 1E-5;delay:time -10.0e-6;
Trigger:A:Type Edge;
Trigger:A:Edge:Source EXT;Coup DC;Slope rise;
Trigger:A:Mode Normal;Level 1.00;
```

THIS PAGE INTENTIONALLY LEFT BLANK

APPENDIX C: BOTH11.TXT

```
RunDig setup file.
Experiment description line

DEVICE:DPO4104:B020141
Digitizer use = VISAR
Factory
Select:CH1 ON;
CH1:Coupling DC;Impedance 50;Pos +4.0;Scale 0.02;
Select:CH2 ON;
CH2:Coupling DC;Impedance 50;Pos +4.0;Scale 0.02;
Select:CH3 ON;
CH3:Coupling DC;Impedance 50;Pos +4.0;Scale 0.02;
Select:CH4 ON;
CH4:Coupling DC;Impedance meg;Pos +4.0;Scale 0.02;
Horiz:RecordLength 100000;Scale 2E-6;delay:time 8.0e-6;
Trigger:A:Type Edge;
Trigger:A:Edge:Source EXT;Coup DC;Slope rise;
Trigger:A:Mode Normal;Level 1.00;

DEVICE:DPO4104:B020142
Digitizer use = pins
Factory
Select:CH1 ON;
CH1:Coupling DC;Impedance meg;Pos +3.0;Scale 1.00;
Select:CH2 ON;
CH2:Coupling DC;Impedance meg;Pos -4.0;Scale 10.0;
Select:CH3 ON;
CH3:Coupling DC;Impedance meg;Pos -4.0;Scale 10.0;
Select:CH4 ON;
CH4:Coupling DC;Impedance meg;Pos +0.0;Scale 0.05;
Horiz:RecordLength 100000;Scale 2E-5;delay:time -10.0e-6;
Trigger:A:Type Edge;
Trigger:A:Edge:Source EXT;Coup DC;Slope rise;
Trigger:A:Mode Normal;Level 1.00;
```

THIS PAGE INTENTIONALLY LEFT BLANK

APPENDIX D: MATLAB CODE FOR SOLVING U_P

```matlab
%% Initial Condition
clc
clear all
rho2=3.85;      %Ceramic
rho1=3.985;      %Sapphire
c1=11.19;
s1=1;
Ud=0.2548;
x1=-4.018:0;
x2=0:6.179;
Us2=14.369
Us2=input('Input the experiment Us found?     ')
%% Coefficient of quadratic equation
a=rho1*s1
b=-(2*rho1*s1*Ud+rho1*c1+rho2*Us2)
c=(rho1*s1*Ud^2+rho1*c1*Ud)
%% Solve quadratic equation
Upx1= -(b + (b^2 - 4*a*c)^(1/2))/(2*a)
Upx2= -(b - (b^2 - 4*a*c)^(1/2))/(2*a)
Up2=input('Upx1 or Upx2 for Up2?     ')
P=rho2*Us2*Up2
```

THIS PAGE INTENTIONALLY LEFT BLANK

GENERAL CARBIDE PRODUCTS ARE MADE IN THE USA

Grade Specifications

GENERALCARBIDE.

	Chemical Composition Weight Percent			Hardness	Density	Average Transverse Rupture
	WC	Co	Other	HRA	g/cm³	Strength (psi)
Tungsten Carbide Grades with Cobalt Binder						
0.6 micron ("submicron")						
GC-012F*	88	12		92.2 - 93.2	14.08 - 14.20	475,000
GC-015F*	85	15		90.8 - 91.8	13.79 - 13.92	560,000
0.8 micron ("submicron")						
GC-005	94.5	5.5		93.4 - 94.2	14.88 - 14.97	445,000
GC-010*	90	10		91.4 - 92.2	14.39 - 14.51	520,000
GC-010CR*	89	10	1	92.3 - 93.3	14.25 - 14.35	530,000
GC-015*	85	15		89.3 - 90.3	13.89 - 14.03	535,000
GC-015CR*	84	15	1	90.4 - 91.4	13.74 - 13.86	550,000
1.0 micron						
GC-103	96.3	3.7		92.7 - 93.5	15.12 - 15.21	480,000
GC-106	94	6		91.9 - 92.7	14.86 - 14.97	510,000
GC-109	91	9		91.0 - 91.8	14.54 - 14.66	525,000
2.0 micron						
GC-206	94	6		91.2 - 92.2	14.86 - 14.97	480,000
GC-209	91	9		90.2 - 91.2	14.53 - 14.65	515,000
GC-211*	89	11		89.4 - 90.4	14.33 - 14.45	530,000
3.0 micron						
GC-310*	90	10		89.3 - 90.3	14.46 - 14.58	510,000
GC-313*	87	13		88.1 - 89.1	14.15 - 14.27	515,000
GC-315*	85	15		87.5 - 88.5	13.95 - 14.09	520,000
GC-320*	80	20		85.6 - 86.6	13.46 - 13.64	470,000
GC-325*	75	25		83.5 - 84.7	13.03 - 13.23	440,000
GC-330*	70	30		81.6 - 82.9	12.61 - 12.82	420,000
6.0 micron						
GC-950*	85	15		86.4 - 87.4	13.95 - 14.09	480,000
GC-618*	82	18		85.2 - 86.2	13.67 - 13.81	450,000
11.0 micron						
GC-915*	85	15		85.6 - 86.6	13.95 - 14.09	440,000
1.0 and 6.0 micron (mixed structure)						
GC-606M	94	6		90.4 - 91.4	14.89 - 15.00	480,000
GC-608M	92	8		89.8 - 90.8	14.66 - 14.78	490,000
GC-610M	90	10		88.8 - 89.8	14.46 - 14.58	500,000
GC-612M	88	12		88.2 - 89.2	14.25 - 14.37	510,000

*Available in Wire EDM Grade

Note: Silicon discounts to the nominal grain size for all grades

SinterHIP Process Guaranteed

THIS PAGE INTENTIONALLY LEFT BLANK

LIST OF REFERENCES

Dandekar, D. P. & Grady, D. E. (2001). Shock equation of state and dynamic strength of tungsten carbide. *Shock Compression of Condensed Matter: 12th APS Topical Conference*, 620, pp. 783–786.

Denzel, J. R. (2010, June). Determination of shock properties of Ceramic Corbit 98: 98% Alumina. Master's thesis, Naval Postgraduate School. Monterey.

Grady, D. E. (1995). *Dynamic Properties of Ceramic Materials.* Sandia National Labs.

Gupta, Y. M., & Ding, J. L. (2002). Impact load spreading in layered materials and structures: Concept and quantitative measure. *Int. J Impact Eng, 27*(3), 277–291.

Gust, W. H., & Royce, E. B. (1971). Dynamic yield strengths of B4C, BeO, and AL2O3 ceramic. *Journal of Applied Physics, 42*(1).

Herrman, W. (1969). Constitutive equation for the dynamic compaction of ductile porous materials. *Journal of Applied Physics ,* 40, 2490–2499.

Ho, C. C. (2009). *Assembly and commissioning of Naval Postgraduate School gas gun for impact studies.* Master's thesis, Naval Postgraduate School. Monterey.

Isbell, W. M. (2005). *Measuring the dynami response of materials.* London: Imperial College Press.

Los Alamos Science. (1985). Shock waves versus sound waves. *Los Alamos Science , Spring/Summer* (12), pp. 42–43.

Marsh, S. P. (1980). *LASL shock hugoniot data.* Los Angeles: University of California Press.

Ong, C. W. (2009). *Investigation of advanced personnel armor using layered construction.* Master's thesis, Naval Postgraduate School. Monterey.

Poh, C. W. (2008). *Investigation of new materials and methods of construction of personnel armour.* Master's thesis, Naval Postgraduate School. Monterey.

Robbins, J. R. Ding, J. L., & Gupta, Y. M. (2004). Load spreading and penetration resistance of layered strucrures – a numerical study. *Int. J Impact Eng., 30*(6), 593–615.

Wikibooks. (2009, Dec 8). *Engineering Acoustics/Qualitative Description of Shock.*
    http://en.Wikibooks.org/wiki
    /Engineering_Acoustics/Qualitative_Description_of_Shocks

Wilkins, M. L. (1978). Mechanics of penetration and perforation. *Int. J. Eng. Sci., 16*,
    793–807.

INITIAL DISTRIBUTION LIST

1.   Defense Technical Information Center
      Ft. Belvoir, Virginia

2.   Dudley Knox Library
      Naval Postgraduate School
      Monterey, California

3.   Professor Young Kwon
      Naval Postgraduate School
      Monterey, California

4.   Professor Jose O. Sinibaldi
      Naval Postgraduate School
      Monterey, California

5.   Professor Yeo Tat Soon
      Temasek Defence System Institute
      National University of Singapore
      Singapore

6.   Tan Lai Poh (Ms), Assistant Manager
      Temasek Defence System Institute
      National University of Singapore
      Singapore